



Characteristics of consecutive tsunamis and resulting tsunami behaviors in southern Taiwan induced by the Hengchun earthquake doublet on 26 December 2006

An-Chi Cheng^{1,2}, Anawat Suppasri^{2,3}, Kwanchai Pakoksung³, and Fumihiko Imamura^{2,3}

¹Civil and Environmental Engineering, Graduate School of Engineering, Tohoku University, 6-6-06 Aoba, Aramaki-Aza, Aoba, Sendai 980-0845, Japan

²WISE Program for sustainability in the Dynamic Earth, Tohoku University, 6-3 Aoba, Aramaki Aza, Aoba, Sendai 980-8578, Japan

³International Research Institute of Disaster Science, Tohoku University, 468-1 Aoba, Aramaki-Aza, Aoba, Sendai 980-0845, Japan

Correspondence: An-Chi Cheng (cheng.anchi.r6@dc.tohoku.ac.jp)

Received: 22 April 2022 – Discussion started: 27 April 2022

Revised: 12 September 2022 – Accepted: 20 January 2023 – Published: 3 February 2023

Abstract. Consecutive M_L 7.0 submarine earthquakes occurred offshore of the Hengchun Peninsula, Taiwan, on 26 December 2006. A small tsunami was generated and recorded at tide gauge stations. This important event attracted public interest, as it was generated by an earthquake doublet and produced a tsunami risk for Taiwan. This study analyzed tide gauge tsunami waveforms and numerical simulations to understand the source characteristics and resulting behaviors of tsunamis. The maximum wave heights at the three nearest stations were 0.08 m (Kaohsiung), 0.12 m (Dongkung), and 0.3 m (Houbihu), and only Houbihu recorded the first wave crest as the largest. The tsunami duration was 3.9 h at Dongkung and over 6 h at Kaohsiung and Houbihu. Spectral analyses detected dominant periodic components of spectral peaks on the tsunami waveforms. The period band from 13.6–23.1 min was identified as the tsunami source spectrum, and the approximate fault area for the consecutive tsunamis was estimated to be 800 km², with central fault depths of 20 km (first earthquake, M_w 7.0) and 33 km (second earthquake, M_w 6.9). The focal mechanisms of the first earthquake, with a strike of 319°, dip of 69°, and rake of –102°, and the second earthquake, with a strike of 151°, dip of 48°, and rake of 0°, could successfully reproduce the observed tsunami waveforms. Numerical simulations suggested that the tsunami waves were coastally trapped on the south coast of Taiwan during the tsunami's passage. The trapped waves propagated along the coast as edge waves, which repeatedly

reflected and refracted among the shelves, interfered with incoming incident wave, and resonated with the fundamental modes of the shelves, amplifying and continuing the tsunami wave oscillation. These results elucidated the generation and consequential behaviors of the 2006 tsunami in southern Taiwan, contributing essential information for tsunami warning and coastal emergency response in Taiwan to reduce disaster risk.

1 Introduction

Taiwan is located at the southeast margin of the Eurasian plate and the Philippine Sea plate. The abrupt movement of plates results in active seismic activity at the boundary area, such as in the Manila Trench and Ryukyu Trench. The Manila Trench and Ryukyu Trench are located offshore of Taiwan and have been identified as hazardous tsunamigenic regions as both have the potential to generate megathrust earthquakes and cause severe tsunami impacts on coastal plains (Liu et al., 2009; Megawati et al., 2009; Wu and Huang, 2009; Li et al., 2016; Qiu et al., 2019; Sun et al., 2018). In addition to potential megathrust earthquakes, historical earthquake tsunamis in Taiwan are well recorded in ancient and written documents. Examples include the 1781/1782 Jiateng Harbor flooding and tsunami event (Li

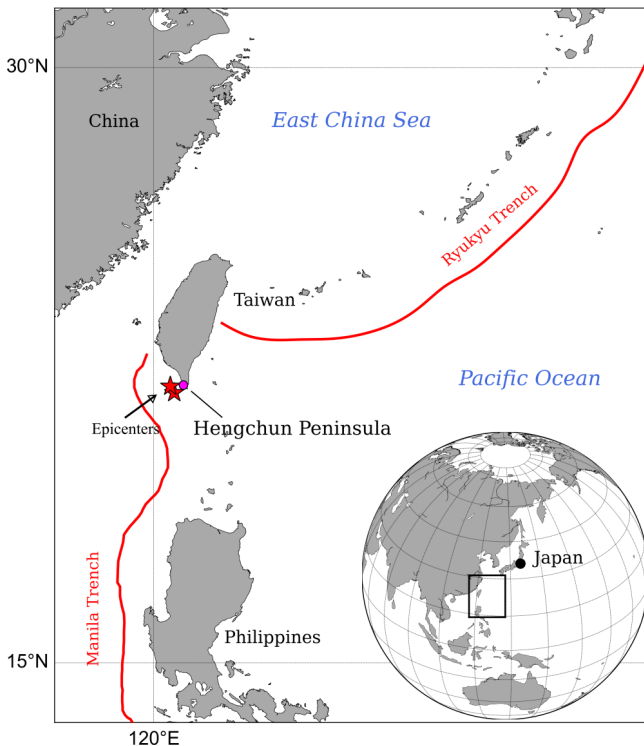


Figure 1. Map of the Hengchun Peninsula, Taiwan. The red stars illustrate the epicenters of the doublet earthquakes, and the solid red lines illustrate the subduction zones of the Manila Trench and the Ryukyu Trench.

et al., 2015; Liu et al., 2022) and the 1867 northern Taiwan earthquake (Cheng et al., 2016; Sugawara et al., 2019).

Two large earthquakes occurred off the coast of Hengchun Peninsula, Taiwan, on 26 December 2006. The first earthquake occurred at 12:26:21 UTC (i.e., 20:26:21 national standard time) and was followed by a second earthquake 8 min later at 12:34:15 UTC (i.e., 20:34:15 national standard time). The Central Weather Bureau (CWB) catalog (R.O.C. – Republic of China) located the epicenter of the first shock at 21.69° N and 120.56° E and that of the second shock at 21.97° N and 120.42° E. The locations of the Hengchun Peninsula and the epicenters of the successive earthquakes are shown in Fig. 1.

The respective magnitudes of these two earthquakes were suggested to be $M_L=7.0$ ($M_w=7.0$ in the Global Centroid Moment Tensor (GCMT) catalog) for the former and $M_L=7.0$ ($M_w=6.9$ in the GCMT catalog) for the latter. From a seismological perspective, pairs of large earthquakes with equivalent fault sizes that occur in similar spatial and temporal proximities are referred to as doublets (Lay and Kanamori, 1980; Kagan and Jackson, 1999). As they shared similar earthquake magnitudes and very close epicenters and occurrence times, the successive earthquakes on 26 December 2006 are considered an earthquake doublet event (Ma and Liang, 2008; Wu et al., 2008). These 2006 earthquakes

in southern Taiwan were considered the largest event in the past 100 years. Several casualties and some structural damages were reported in southern Taiwan during this seismic event (Wu et al., 2009). The tectonic settings of the 2006 earthquake doublet are shown in Fig. 2.

A small tsunami was generated after the successive strong motions of these earthquakes. The tsunami propagated toward and reached the western coast of southern Taiwan immediately after the earthquakes. Although no coastal run-up or inundation was reported, tsunami signals were instrumentally recorded at CWB tide gauge stations in southern Taiwan for the first time. The December 2006 tsunami was an important event that attracted public interest, as it was unique not only because it was generated by earthquakes in short succession but also because it was a new occurrence for ordinary citizens in Taiwan. This recent tsunami not only corroborates the tsunami risk in Taiwan but also increases awareness of the need for disaster risk management, such as preparedness and mitigation countermeasures for future tsunamis.

The tsunami observations that were reported following the 26 December 2006 tsunami also raised some questions. First, the first tsunami wave crest was not shown to be the largest at some stations. This amplified tsunami wave is considered an important issue for tsunami warnings, as a higher later wave could suddenly upgrade the threat level of the tsunami (Suppasri et al., 2017). Second, the tsunami oscillation recorded at some stations lasted for more than 6 h following the earthquakes. This indicated that the high-energy waves persisted along the coast without decay during the 2006 tsunami and were considered one of the cascading risks of tsunamis, as they could further intensify the damaging impacts of the tsunamis on the coastal region.

The other issue was to identify which source models could better explain the successive tsunamis compared to the recorded observations in southern Taiwan. Wu et al. (2008) simulated the tsunami from this event using several possible fault plane mechanisms. They numerically computed the tsunami propagation on three nested grids and compared their simulated tsunami waveforms with observational data from tide gauge stations. Although the source models for this tsunami event have been specified and modeled in previous studies, the uncertainty and variability aspects of these models and the bathymetry have not been thoroughly investigated. These uncertainties in earthquake fault parameters and significant differences among open-source bathymetries can exaggerate the modeled results compared to the predictions of previous studies of the 2006 tsunami. Therefore, it is critical to discuss these model performances from a sensitivity perspective because it is desirable to obtain a tsunami source model and understand the reliability of bathymetry data that are utilized for numerical simulation to reasonably estimate the tsunami wave activities of the 2006 tsunami.

Based on the above background, the primary intent of this article is to address all aforementioned issues related to the 2006 tsunami that have not been previously discussed and to

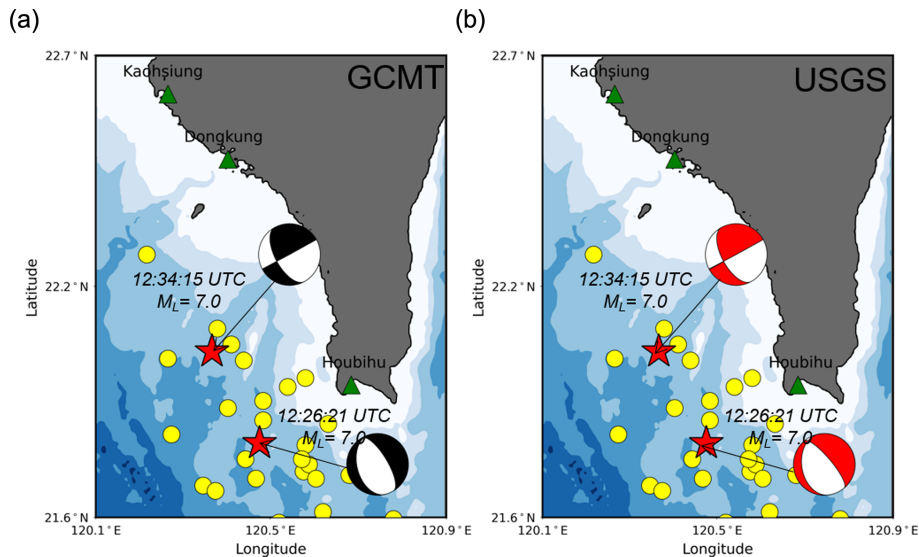


Figure 2. The tectonic settings of the 2006 earthquake doublet. The red stars denote the epicenters of the successive earthquakes. The beach balls denote the focal mechanisms of the two earthquakes estimated from the GCMT and USGS moment tensor solutions. The yellow circles show the aftershock distribution for 1 d from the USGS earthquake catalog. The green triangles represent the locations of the CWB tide gauge stations.

provide some results. The content of this article is organized as follows. First, the observed tsunami waveforms are analyzed to determine the physical characteristics of the tsunami and employed as inputs for root mean square (RMS) analyses to detect the tsunami duration. Second, spectral analyses are performed to detect the periodic components of the tsunami waves based on the identification of the tsunami source spectrum and resonance modes. Then, a sensitivity analysis of the source models and open-source bathymetries is conducted based on the simulated waveforms from forward tsunami simulations. The mechanism of tsunami wave trapping around southern Taiwan is examined based on the comparison of modeled results from numerical experiments using real and manipulated bathymetry. The December 2006 earthquake tsunami represents a unique and recent incident in Taiwan; therefore, this reconstruction and these findings could not only help further clarify tsunami generation and the important behaviors responsible for tsunami hazards facing the island of Taiwan but also have implications for tsunami warning and disaster risk management.

2 Data and methods

2.1 Tide gauge tsunami data

Time history data of sea levels that are recorded at coastal sites provide one source of information that we can use to study tsunami patterns. To investigate the characteristics of the 2006 tsunami, sea level records from tide gauge stations were employed for analysis in the present study. For this purpose, the recorded data from three tide gauge stations (Kaoh-

siung, Dongkung, and Houbihu) located in southern Taiwan were obtained. These tide gauge stations are operated and maintained by the CWB, R.O.C. All stations recorded sea levels at a sampling interval of 6 min. In this doublet event, the first and second earthquakes occurred at 20:26:21 and 20:34:15 (national standard time), respectively. Hence, 28 h of tide gauge records (from 08:00 on 26 December 2006 to 12:00 on 27 December 2006, national standard time) were adopted for analysis. To approximate the wave components of the tsunami and to remove the low-frequency noise that was attributed to the tidal effect, the sea level records at the tide gauge stations were de-tided by removing the long-period (> 2 h) tidal constituents. The original data recorded at the tide gauge stations in southern Taiwan are shown in Fig. 2a, and the de-tided data are presented in Fig. 2b. The locations of the tide gauge stations are shown in Fig. 3.

The tsunami duration represents the observation time of high-energy tsunami waves persisting at a coastal site. The tsunami durations at all the stations were identified based on a calculation of root mean square (RMS) sea levels, indicating the elapsed time of the wave amplitude above the normal oscillation level before the tsunami wave arrived (Hayashi et al., 2012; Heidarzadeh and Satake, 2014; Heidarzadeh et al., 2019, 2021). The RMS analysis calculated the moving average of the recorded sea level along a moving time window of 24 min. The calculation for RMS sea level is presented in Eq. (1).

$$S(t) = \sqrt{\frac{1}{w} \int_{t-\frac{w}{2}}^{t+\frac{w}{2}} h(x)^2 dx} \quad (1)$$

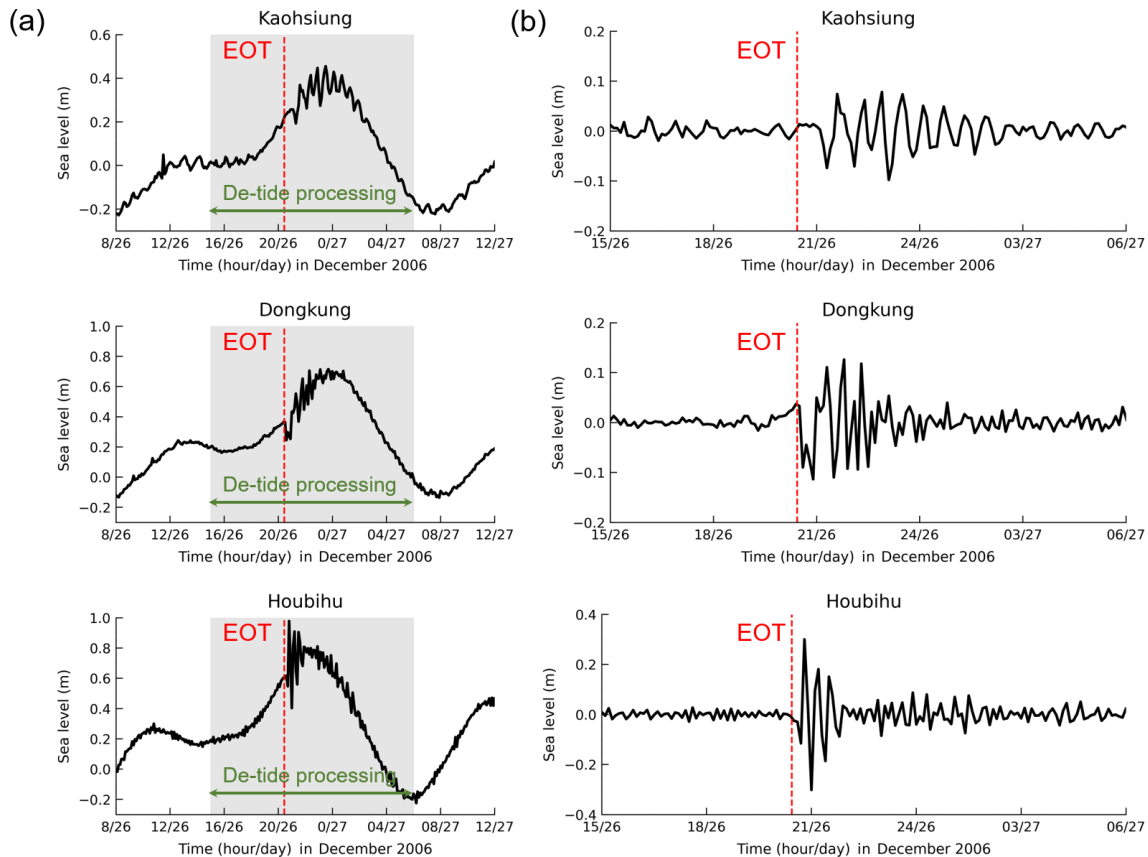


Figure 3. The (a) original and (b) de-tided sea levels recorded at tide gauge stations in southern Taiwan during the 26 December 2006 tsunami event. The vertical, dashed red lines indicate the earthquake occurrence time (EOT). The gray shaded areas illustrate the tide gauge data used for de-tide processing. The data shown in the graphs were drawn based on national standard time.

In this equation, $S(t)$ represents the RMS sea level at time step t , $h(t)$ denotes the recorded sea level at time t , and w stands for the moving time window. In the present study, the length of the tsunami data employed for RMS analysis is 12 h, which includes 120 data points, ranging from 17:00 on 26 December 2006 to 05:00 on 27 December 2006 (national standard time).

2.2 Spectral analyses

To apply spectral analyses to the tsunami data, two types of analyses were included and processed in this study: Fourier analysis and wavelet (time–frequency) analysis. The Fourier analysis is based on the fast Fourier transform (FFT) algorithm and applied based on the updated open-source library, NumPy, in the Python package (Harris et al., 2020). Fourier analysis was performed to estimate the spectral components of the time history data of the tsunami waveform. The entire dataset of the tsunami waveform inputted for Fourier analysis covered 600 min, which included 100 data points ranging from 5 h before to 5 h after the tsunami, as the sampling rate of the data was 6 min. The Fourier analysis was separately applied to the de-tided background (i.e., 5 h data before the

tsunami arrival) and the tsunami signals (i.e., 5 h data after tsunami arrival) to identify significant changes in the spectral energy associated with the tsunami. Additionally, the spectral ratio was computed for the tsunami spectra to exclude the local modes of coastal sites from the periodic components. Wavelet analysis was computed based on the Morlet mother function (Torrence and Compo, 1995). Wavelet analysis detects the periodic change in spectral peaks over time. The length of the tsunami data input in the wavelet analysis was 15 h (15:00 on 26 December 2006 to 06:00 on 27 December 2006, national standard time). A similar method has been widely applied to solve time–frequency problems for many tsunami events, such as the 1945 Makran earthquake tsunami and the 2020 Alaska earthquake tsunami (Heidarzadeh and Satake, 2015; Heidarzadeh and Mulia, 2021).

2.3 Numerical tsunami simulation

Numerical simulation is a computer-based method that describes equations for the motion of tsunami wave propagation. Tsunami wave propagation can be numerically modeled based on various theories, including shallow water and dispersive wave theories. Among those theories, the shallow wa-

ter equations are some of the most commonly used methods to model tsunami propagation from the source to nearshore areas. Various computational models have been developed to solve shallow water equations, and the TUNAMI (Tohoku University Numerical Analysis Model for Investigation of tsunamis) code is one of the widely used models to numerically simulate both far-field and near-field tsunamis (Suppasri et al., 2012, 2014). The second version of the TUNAMI code (TUNAMI-N2) was mainly developed to deal with near-field tsunamis by applying the nonlinear theory of shallow water equations, which is solved using a leap-frog scheme (Imamura, 1995). Since the 2006 tsunami presented as a near-field tsunami in Taiwan, the TUNAMI-N2 model was used in this study to simulate the 2006 tsunami with nonlinear shallow water equations. The nonlinear shallow water equations on the Cartesian coordinate system are presented in Eqs. (2)–(4), and the nonlinear equations are solved by applying the finite difference method.

$$\frac{\partial \eta}{\partial t} + \frac{\partial M}{\partial x} + \frac{\partial N}{\partial y} = 0 \quad (2)$$

$$\begin{aligned} \frac{\partial M}{\partial t} + \frac{\partial}{\partial x} \left(\frac{M^2}{D} \right) + \frac{\partial}{\partial y} \left(\frac{MN}{D} \right) + gD \frac{\partial \eta}{\partial x} \\ + \frac{gn^2}{D^{7/3}} M \sqrt{M^2 + N^2} = 0 \end{aligned} \quad (3)$$

$$\begin{aligned} \frac{\partial N}{\partial t} + \frac{\partial}{\partial x} \left(\frac{MN}{D} \right) + \frac{\partial}{\partial y} \left(\frac{N^2}{D} \right) + gD \frac{\partial \eta}{\partial y} \\ + \frac{gn^2}{D^{7/3}} N \sqrt{M^2 + N^2} = 0 \end{aligned} \quad (4)$$

In these equations, η is the water level, M and N are the discharge fluxes in the x and y directions, respectively, D is the total water depth, g is the gravitational acceleration, and n is Manning's roughness coefficient. The bottom friction term was represented by the Manning roughness coefficient, which was set as $0.025 \text{ s m}^{-1/3}$, assuming that the seafloor in the model domain is in perfect condition. The numerical tsunami simulations were conducted with a time interval of 0.1 s and grid intervals of 450 m. The entire model domain covered the source region and southern Taiwan, which comprised mesh numbers of 538 and 631 in the x and y directions, respectively. The time interval and grid intervals were set up to satisfy the Courant–Friedrichs–Lewy (CFL) condition to ensure the stability of the simulation. The CFL condition is presented in Eq. (5):

$$\Delta t \leq \frac{\Delta x}{\sqrt{2gh_{\max}}}, \quad (5)$$

where Δt is the time interval, Δx is the grid spacing, and h_{\max} is the maximum water depth in the model domain. As the initial condition inputted for numerical tsunami simulation, the initial water level distribution was calculated from the earthquake fault parameters using Okada's theory

(Okada, 1985). In addition, the horizontal deformation contribution to tsunami generation on steep bathymetric slopes was included (Tanioka and Satake, 1996). The calculation conditions for the numerical tsunami simulation are summarized in Table 1.

2.4 Sensitivity analyses of source models

2.4.1 Single fault models

Multiple forward tsunami simulations were conducted using single fault models with different fault depths and fault orientations. The main goal of the multiple forward tsunami simulations was to find a single fault model that could produce tsunami waveforms that were highly consistent with the tide gauge station observations in southern Taiwan.

There were two moment tensor solutions available from the Global Centroid Moment Tensor (GCMT) project and United States Geological Survey (USGS) for the successive earthquakes on 26 December 2006 (Fig. 2). Each solution suggested two possible fault planes for those earthquakes. The focal mechanisms for the two earthquakes estimated by the GCMT and USGS are summarized in Table 2.

Through the analysis of the tsunami waveforms simulated by the multiple forward tsunami simulations, one of those fault planes could be chosen as the appropriate fault plane for the respective earthquakes of the 2006 earthquake doublet. A similar approach has been applied in a previous study to obtain the optimum fault plane for the 2016 Fukushima normal faulting earthquake (Gusman et al., 2017).

Wu et al. (2008) computed synthetic tsunami waveforms based on single fault models using different fault planes of the GCMT solutions. They found that the nodal plane (NP) of NP2 of the first earthquake, with a strike of 329° , dip of 61° , and rake of -98° , and the fault plane of NP1 for the second earthquake, with a strike of 151° , dip of 48° , and rake of 0° , produced tsunami waveforms that better fit the observed data.

Based on the study conducted by Wu et al. (2008), the focal mechanisms of NP2 for the first earthquake and NP1 for the second earthquake from the GCMT solution were used for a sensitivity analysis of fault depths. An approximated fault area 40 km long and 20 km wide (800 km^2) was estimated for the successive earthquakes based on the empirical formula with tsunami source periods. The methods by which the fault area of the two earthquakes was obtained are discussed in Sect. 4.1. For the given moment magnitude (M_w) values of the 7.0 and 6.9 earthquakes, the amount of average slip can be estimated to be 1.66 m for the first earthquake (i.e., M_w 7.0) and 1.17 m for the second earthquake (M_w 6.9), assuming a rigidity of 30 GPa. The centroid depths of the GCMT (20 km) and USGS (25 km) solutions for the first earthquake are significantly different, while a similar depth of 33 km was estimated from both solutions for the second earthquake. Therefore, for the sensitivity analysis of central

Table 1. Calculation conditions for the numerical tsunami simulation.

Calculation condition for the numerical tsunami simulation	
Governing equation	Two-dimensional nonlinear shallow water equations (TUNAMI-N2 model)
Numerical integration method	Leap-frog finite difference method
Initial condition	Initial water level calculated from fault parameters using the theory of Okada (1985) considering the contribution of horizontal coseismic displacement
Coordination system	Cartesian coordinate system
Boundary condition	Radiation boundary condition
Stability criterion	Courant–Friedrichs–Lewy (CFL) condition
Time interval	0.1 s
Mesh size	450 m
Mesh number (x, y)	(538, 631)

Table 2. Focal mechanisms for successive earthquakes estimated by GCMT and USGS.

		Earthquake 1		Earthquake 2	
		NP1	NP2	NP1	NP2
GCMT	Long (° E)	120.52		120.4	
	Lat (° N)	21.81		22.02	
	Strike (°)	165	329	151	61
	Dip (°)	30	61	48	90
	Rake (°)	−76	−98	0	138
	Depth (km)	20		33	
	USGS	Long (° E)	120.55		120.49
Lat (° N)		21.8		21.97	
Strike (°)		171	319	151	61
Dip (°)		24	69	48	90
Rake (°)		−61	−102	0	138
Depth (km)		25		33	

fault depth, the central fault depths of 15, 20, 25, and 35 km of the first earthquake were evaluated.

After determining the best central fault depth for the single fault models of the two earthquakes, multiple tsunami forward simulations were applied to all possible fault planes from the moment tensor solutions estimated by GCMT and USGS using a single fault model. The misfit of observed and simulated tsunami waveforms from the multiple tsunami forward simulations was calculated and compared to examine the focal mechanisms that better explain the observed tsunami data. The misfit of the observed and simulated tsunami waveforms can be calculated using Eq. (6):

$$\varepsilon = \frac{1}{N} \sqrt{\sum_{i=1}^N \frac{(\text{Obs}_i - \text{Sim}_i)^2}{(\text{Obs}_i)^2}}, \quad (6)$$

where ε is the misfit of the observed and synthetic tsunami waveforms, N is the total number of data points, Obs_i is the observed data at time step i , and Sim_i is the simulated data at time step i . Equation (6) calculates ε for one station. For cases with several stations, the overall misfit is obtained from the mean of the ε values computed from all the stations.

2.4.2 Multiple fault models

After determining the best central fault depths and fault orientations of a single fault, the area of each single fault was subdivided into eight subfaults with areas of $10 \text{ km} \times 10 \text{ km}$, with four and two subfaults along the strike and dip axes, respectively. The locations of each subfault in the fault model of the two earthquakes are shown in Fig. 4. The top depths for the two earthquakes are 15.3 and 29.1 km, which correspond to subfaults 1–4 in each fault model (Fig. 4a, b). The rest of the depths from the shallowest to the deepest portion along the dip axis are derived using fault parameters of width dimensions and dip angles. The respective fault parameters of each subfault in the fault models of the two earthquakes are summarized in Table 3.

The tsunami sensitivity to the non-uniform slip distribution of the fault model was evaluated. For that purpose, two slip levels for each subfault were established, namely the large (asperity) slip and the background slip region of the entire fault. The large slip and background slip region should satisfy the M_w to avoid overestimation. The slip amount in each region was obtained using the following procedures. First, the amount of average slip (D_a) was calculated using the M_w , the entire fault area (S), and a rigidity (μ) of 30 GPa, per Eqs. (7)–(8) introduced by Kanamori and Anderson (1975).

$$M_w = \frac{\log M_0 - 9.1}{1.5} \quad (7)$$

Table 3. Parameters of the subfaults for the two earthquakes of the 2006 earthquake doublet.

	Sub fault	Long (° E)	Lat (° N)	Length (km)	Width (km)	Depth (km)	Strike (°)	Dip (°)	Rake (°)
Earthquake 1	1	120.619	21.588	10	10	15.3	319	69	-102
	2	120.556	21.657	10	10	15.3	319	69	-102
	3	120.492	21.724	10	10	15.3	319	69	-102
	4	120.429	21.792	10	10	15.3	319	69	-102
	5	120.692	21.648	10	10	24.7	319	69	-102
	6	120.629	21.716	10	10	24.7	319	69	-102
	7	120.565	21.784	10	10	24.7	319	69	-102
	8	120.501	21.852	10	10	24.7	319	69	-102
Earthquake 2	1	120.726	21.989	10	10	29.1	151	48	0
	2	120.642	21.946	10	10	29.1	151	48	0
	3	120.557	21.902	10	10	29.1	151	48	0
	4	120.473	21.858	10	10	29.1	151	48	0
	5	120.680	22.068	10	10	29.1	151	48	0
	6	120.595	22.024	10	10	36.5	151	48	0
	7	120.510	21.980	10	10	36.5	151	48	0
	8	120.426	21.936	10	10	36.5	151	48	0

$$D_a = \frac{M_0}{\mu S} \tag{8}$$

Next, the amount of large slip ($2D_a$) was assumed to be twice that of the average slip. The total area of the large slip area (S') was set to be 25 % of the entire fault area, and the seismic moment of the large slip area (M'_0) can be obtained using Eq. (8). Then, the slip amount of the background area (D_b) can be estimated using the area of the background region (S_b) following Eqs. (9)–(10).

$$S_b = S - S' \tag{9}$$

$$D_b = \frac{M_0 - M'_0}{\mu S_b} \tag{10}$$

The details of the slip amount in each region for the two earthquakes are summarized in Table 4a.

After determining the slip amount of the asperity and background regions, the tsunami sensitivity to the asperity location was studied. The asperity area with the large slip was assumed at the shallow portion of the entire fault area, focusing on the north (subfaults 3–4), central (subfaults 2–3), and south (subfaults 1–2) parts of each earthquake fault model. Assuming different asperity locations for the two earthquakes, a total of nine scenarios were simulated. The multiple fault models and the generated tsunamis of each earthquake are shown in Figs. 5 and 6. The asperity locations of multiple fault models for the two earthquakes in each scenario are summarized in Table 4b.

Table 4. (a) Details of the average slip, large slip, and background slip for the two earthquakes. (b) Asperity locations of multiple fault models for the two earthquakes.

(a)						
	Earthquake 1	Earthquake 2				
Moment magnitude (M_w)	7.0	6.9				
Entire fault size (km ²)	800	800				
Rigidity (GPa)	30	30				
Average slip D_a (m)	1.66	1.17				
Large slip $2D_a$ (m)	3.32	2.35				
Background slip (m)	1.11	0.78				
(b)						
Scenario	Asperity location of earthquake 1			Asperity location of earthquake 2		
	North	Central	South	North	Central	South
LS1	○				○	
LS2		○			○	
LS3			○		○	
LS4	○			○		
LS5		○		○		
LS6			○	○		
LS7	○					○
LS8		○				○
LS9			○			○

2.5 Tsunami simulation using open-source bathymetry data

In addition to the fault parameters of the source models, bathymetry data are needed for simulating tsunami wave propagation. Simulated tsunami propagation results

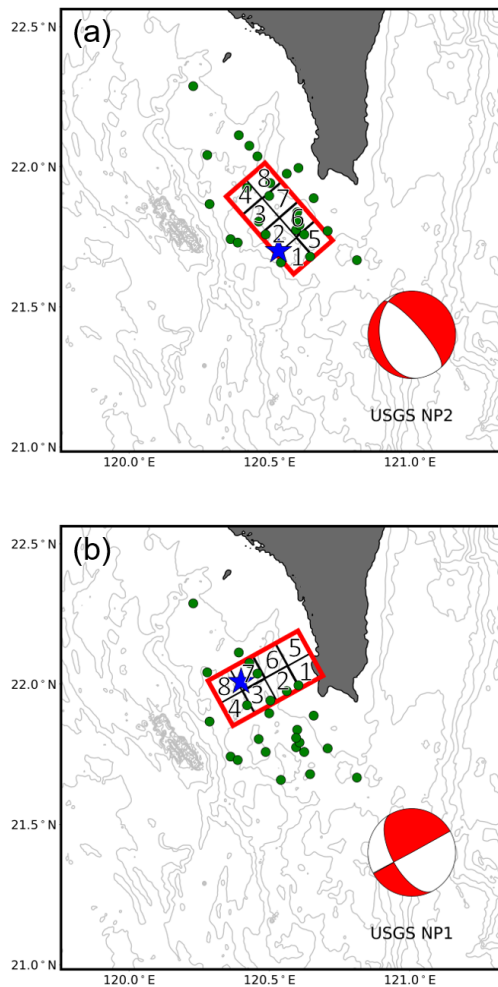


Figure 4. Fault models for the two earthquakes. **(a)** Subfault locations of the first earthquake (M_w 7.0) using NP2 of USGS's moment tensor solution. **(b)** Subfault locations of the second earthquake (M_w 6.9) using NP1 of USGS's moment tensor solution.

are known to be sensitive to the accuracy and resolution of bathymetry data. Although it can be expected that bathymetry data with a higher accuracy and resolution can produce simulated results that better fit the actual values, such data are not always available and freely accessible. Due to this limitation, open-source datasets have often been utilized for modeling tsunamis in many previous studies (Koshimura et al., 2008; Li et al., 2016; Otake et al., 2020; Wang et al., 2022; Ren et al., 2022).

Unfortunately, open-source datasets are sometimes problematic and insufficient for the accurate simulation of tsunami waves because they lack accurate, quality data (Griffin et al., 2015). A similar issue has been reported by previous studies in simulating the 2018 Sulawesi tsunami and the 2018 Anak Krakatoa tsunami (Heidarzadeh et al., 2019; Zengaffinen et al., 2020). Significant differences in various sources of datasets can also result in modeled results

that contrast estimated values from previous studies. Therefore, for the purpose of tsunami hazard assessment, it is important to assess and note different available open-source bathymetries in relation to model performances, using the 2006 tsunami as an example.

For this purpose, a tsunami simulation was separately applied to two different sources of bathymetry data, namely General Bathymetric Chart of the Oceans (GEBCO) data and ETOPO1 data, and the misfit between the modeled results was evaluated. The GEBCO data contain bathymetry data with grid intervals of 15 arcsec, while ETOPO1 data have sea depth data with a resolution of 1 arcmin. To fairly investigate the model performances from different datasets, bathymetry data from the two datasets were converted to 450 m grids and used as the input for the numerical tsunami simulations. Figure 7 shows the bathymetry data of the modeled domain obtained from GEBCO and ETOPO1 data. As the initial condition, the initial water distribution of the tsunami generated by the proposed multiple fault model (LS2) was used for these simulations, in which the asperity locations of the two earthquakes were assumed to be at the center of the entire fault area.

2.6 Evaluation of the bathymetry effect on tsunami wave trapping

To examine any significant change in tsunami wave transmission that could be attributed to the bathymetry effect during the passage of the 2006 tsunami, numerical experiments (MS, EXP1, EXP2) for tsunami propagation were conducted using actual and manipulated bathymetry data. For the main simulation (MS) numerical experiment, actual GEBCO bathymetry data with a resolution of 450 m derived from sea depth data with grid intervals of 15 arcsec were used. For the manipulated bathymetry data that were used for numerical experiment EXP1, sea depths greater than 500 m were replaced with 500 m depths. For numerical experiment EXP2, the bathymetry data were manipulated by removing sea depth data with a flattened sea bottom at a depth of 500 m. The 500 m depth was specified because the bathymetric slopes are very gentle at sea depths shallower than 500 m near southern Taiwan, and the area is therefore considered a shelf region. Figure 8 shows the map-manipulated bathymetry of the model domain for numerical experiments EXP1 and EXP2. The details of the bathymetry data used for numerical experiments MS, EXP1, and EXP2 are summarized in Table 5.

The results of the numerical experiments were compared to examine how tsunami wave directivity could change due to the bathymetric effect and to evaluate how much tsunami wave energy could be coastally trapped in different bathymetric conditions during the passage of the 2006 tsunami.

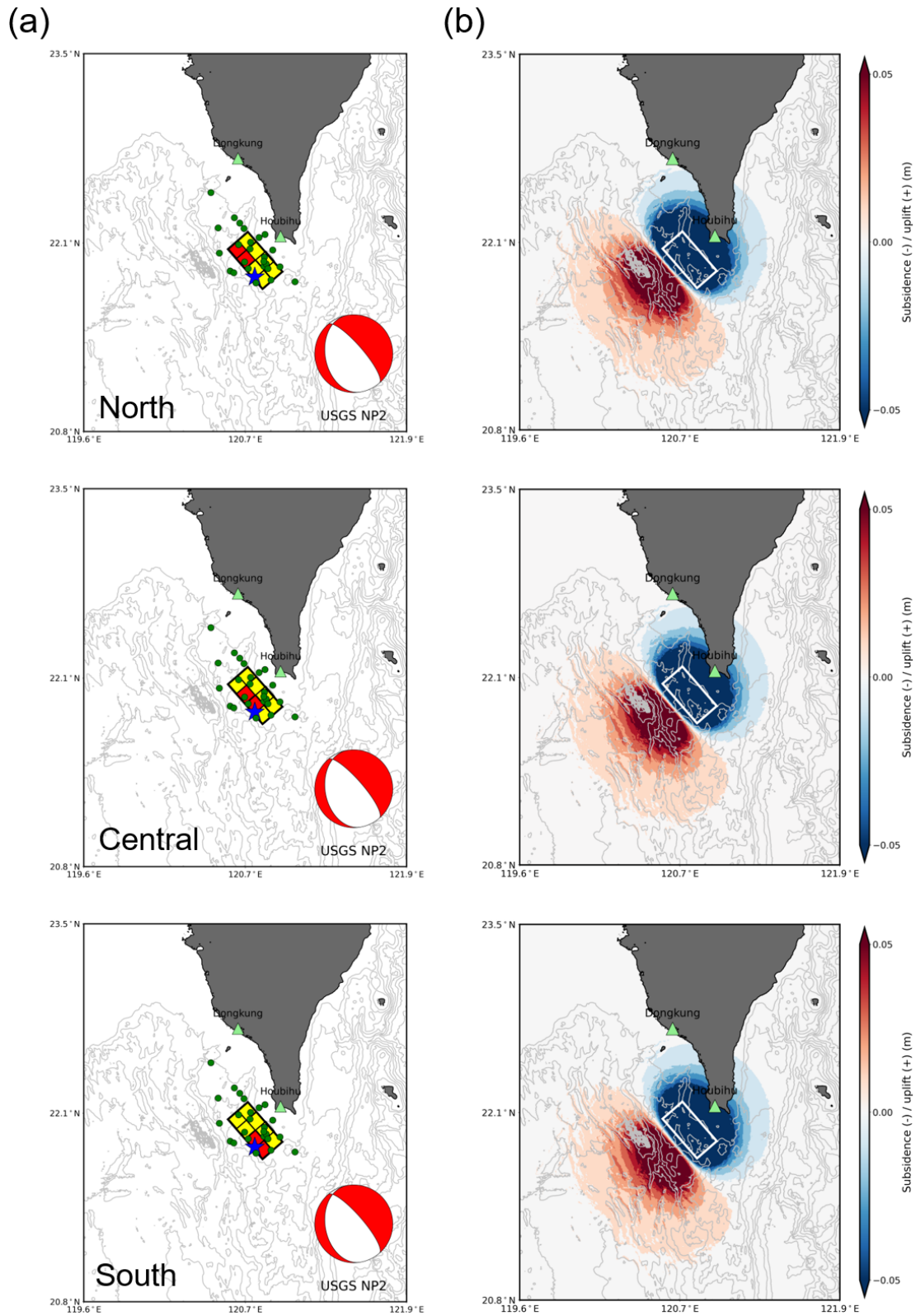


Figure 5. (a) Map of subfault boundaries with different asperity locations for the first earthquake (M_w 7.0). (b) Coseismic crustal vertical displacement calculated using the fault parameters of the subfaults. The beach ball denotes the focal mechanisms of USGS’s NP2 nodal planes for the first earthquake. The subfaults in red represent large slip areas, and the subfaults in yellow represent background slip areas. The large slip area was located only at the shallow part of the entire fault area. The blue stars represent the epicenter of the first earthquake, and the green circles represent the aftershocks. The tide gauge stations are plotted as green triangles.

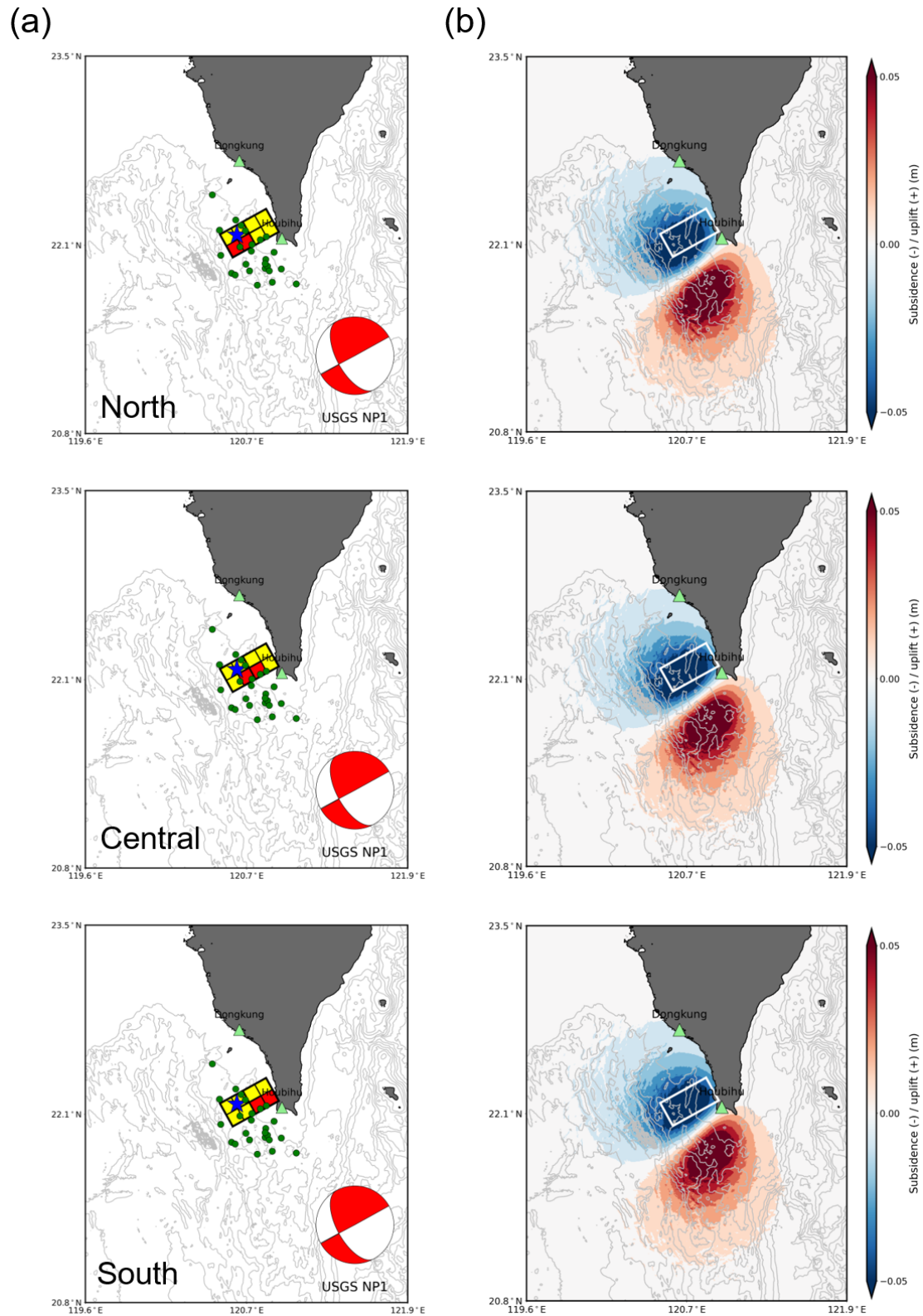


Figure 6. (a) Map of subfault boundaries with three different locations of large slip areas for the second earthquake (M_w 6.9). (b) Coseismic crustal vertical displacement calculated using the fault parameters of the subfaults. The beach ball denotes the focal mechanisms of USGS's NP2 nodal planes for the first earthquake. The subfaults in red represent large slip areas, and the subfaults in yellow represent background slip areas. The large slip area was located only at the shallow part of the entire fault area. The blue stars represent the epicenter of the first earthquake, and the green circles represent the aftershocks. The tide gauge stations are plotted as green triangles.

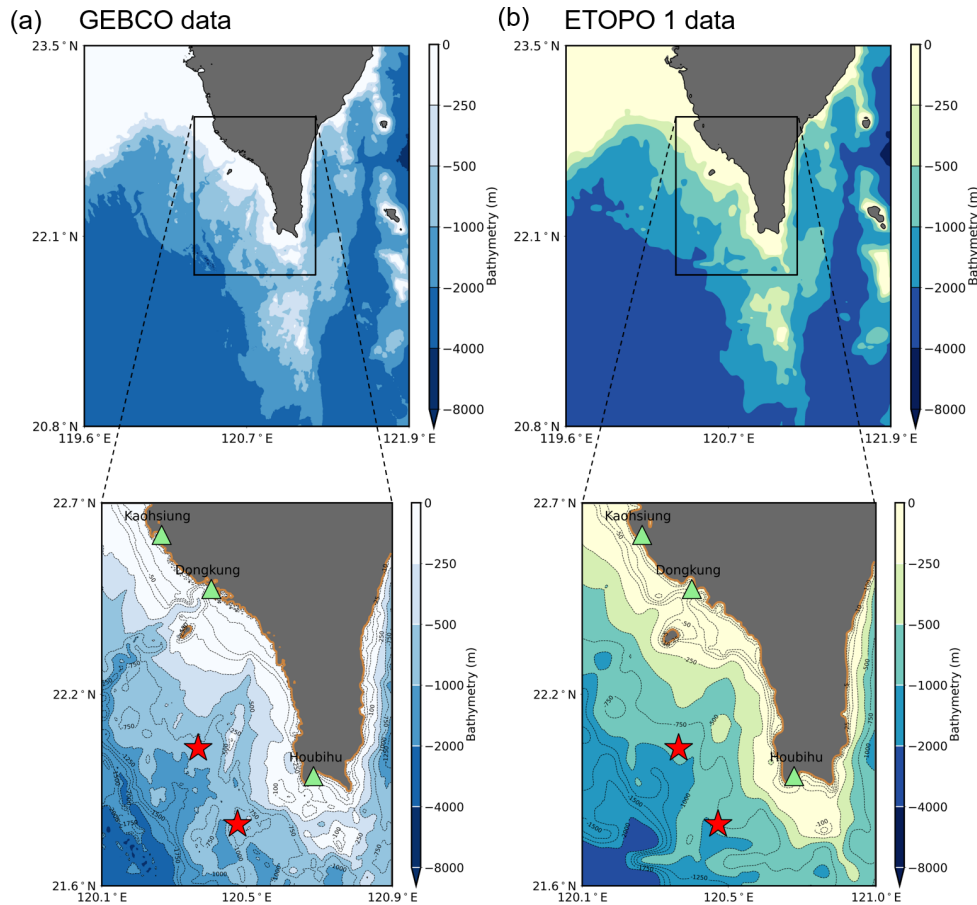


Figure 7. Bathymetry map of the model domain from GEBCO and ETOPO1 bathymetry data. The green triangles denote the locations of the tide gauge stations. The red stars represent the epicenters of the two earthquakes.

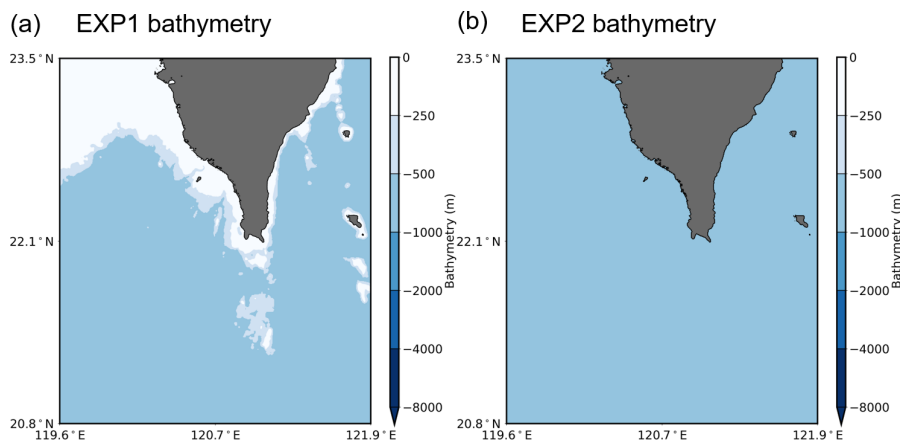


Figure 8. Maps of the manipulated bathymetry of the model domain for numerical experiments (a) EXP1 and (b) EXP2.

3 Analyses of tsunami waveforms and durations

3.1 Physical characteristics of tsunami waveforms

The December 2006 earthquake tsunami was observed at several tide gauges located along the southwestern coast of

Taiwan. The tsunami observations are plotted in Fig. 9a. The initial wave arrived at all three tide stations in southern Taiwan with an amplitude sign of a trough wave. The travel times of the initial wave to all the stations were recorded: 16 min to Houbihu, 28 min to Dongkung, and 52 min to

Table 5. Details of the bathymetry data used for the numerical experiments MS, EXP1, and EXP2.

	Numerical experiments		
	MS	EXP1	EXP2
Bathymetry source	GEBCO data		
Grid size	450 m		
Mesh number (x, y)	(538, 631)		
Description of bathymetry conditions	Sea depths from GEBCO data	Sea depths larger than 500 m were replaced with 500 m depths	Sea depths of entire domain were replaced with 500 m depths.

Kaohsiung. The initial wave was recorded as -0.12 m in Houbihu, -0.09 m in Dongkung, and 0.06 m in Kaohsiung. Following the trough sign of the initial wave, the first wave crest record at Houbihu was 0.3 m, which was approximately 3 times greater than that at Dongkung and 4 times larger than that at Kaohsiung. This was natural because Houbihu was the station closest to the epicentral region and therefore had an earlier arrival time and was relatively sensitive to the surface elevation change in sea level that was induced by the tsunami. The maximum wave heights were recorded as 0.08 m (Kaohsiung), 0.12 m (Dongkung), and 0.3 m (Houbihu). In Kaohsiung and Dongkung, the maximum height was not recorded for the initial wave. The maximum wave height appeared 36 min after the initial wave arrived at Kaohsiung and after 24 min at Dongkung, indicating a pattern of wave amplification at these stations. These results suggest that different propagation effects existed at these coastal sites during the passage of the 2006 tsunami. In addition to significant differences in wave amplitude and arrival time, the tsunami records at each station also varied in terms of visible wave periods. The visible period of the tsunami wave at Kaohsiung was recorded from 30–48 min based on the tsunami waveform, which was approximately 2 times longer than those observed at Dongkung and Houbihu (from 18–24 min). This indicated that wave components with shorter periods were not well recorded in Kaohsiung. The locations and details of the tide gauge observations are summarized in Table 6a for wave amplitude and Table 6b for arrival time and visible period.

3.2 Tsunami durations

Another issue was to determine the tsunami duration at each station because it can help to identify the length of wave oscillations at a coastal site due to the tsunami. Typically, the tsunami duration describes the elapsed time during which a high-energy wave at a tide gauge station exceeds the mean sea level of a normal oscillation. The normal oscillation was defined as the site-specific oscillation at each station before the tsunami arrived. RMS analysis was applied to the recorded sea level data at each station. The results of the RMS analysis are plotted in diagrams shown in Fig. 9b.

The RMS sea level diagram illustrates how long the high-energy wave persisted at each station. Accordingly, the tsunami duration was determined through a comparison of the RMS sea level and the basic oscillation in sea level at each station. The maximum RMS sea level derived at the Houbihu station was estimated to be 2–3 times higher than those at the Dongkung and Kaohsiung stations. The calculated tsunami duration at Dongkung was as much as 3.9 h, while the tsunami continued for more than 6 h in Kaohsiung and Houbihu.

Generally, several oscillation modes are expected to be induced during a tsunami event associated with the tsunami source, propagation path, and topographic effects (Rabinovich, 1997; Rabinovich et al., 2013). An island setting such as Taiwan, where continental shelves and gentle slopes exist, commonly traps waves over the shelf during the passage of tsunamis (Munger and Cheung, 2008; Roeber et al., 2010). The trapped waves propagate along the coastline and normally trigger various oscillation modes in the coastal water due to the interference of wave reflection at the edge of the continental shelves (Yamazaki and Cheung, 2011). The wave resonance of these oscillation modes with the fundamental modes can enhance coastal hazards with amplified amplitudes and long tsunami durations (Tanioka et al., 2019; Yamanaka and Nakamura, 2020; Wang et al., 2021, 2022). The triggered oscillation modes are expected to be mixed with the tsunami source spectrum in the observation records from the coastal sites. To identify these modes from the tsunami source spectrum, spectral analyses were performed on the observation records at all three tide gauge stations in southern Taiwan, as detailed in the next section.

4 Spectral analysis

4.1 Tsunami source spectra

To examine the spectral characteristics of the tsunami waves, Fourier analysis was applied to 10 h of de-tided observed data (i.e., 5 h before and after the tsunami's arrival) that were recorded at all the tide gauge stations in southern Taiwan.

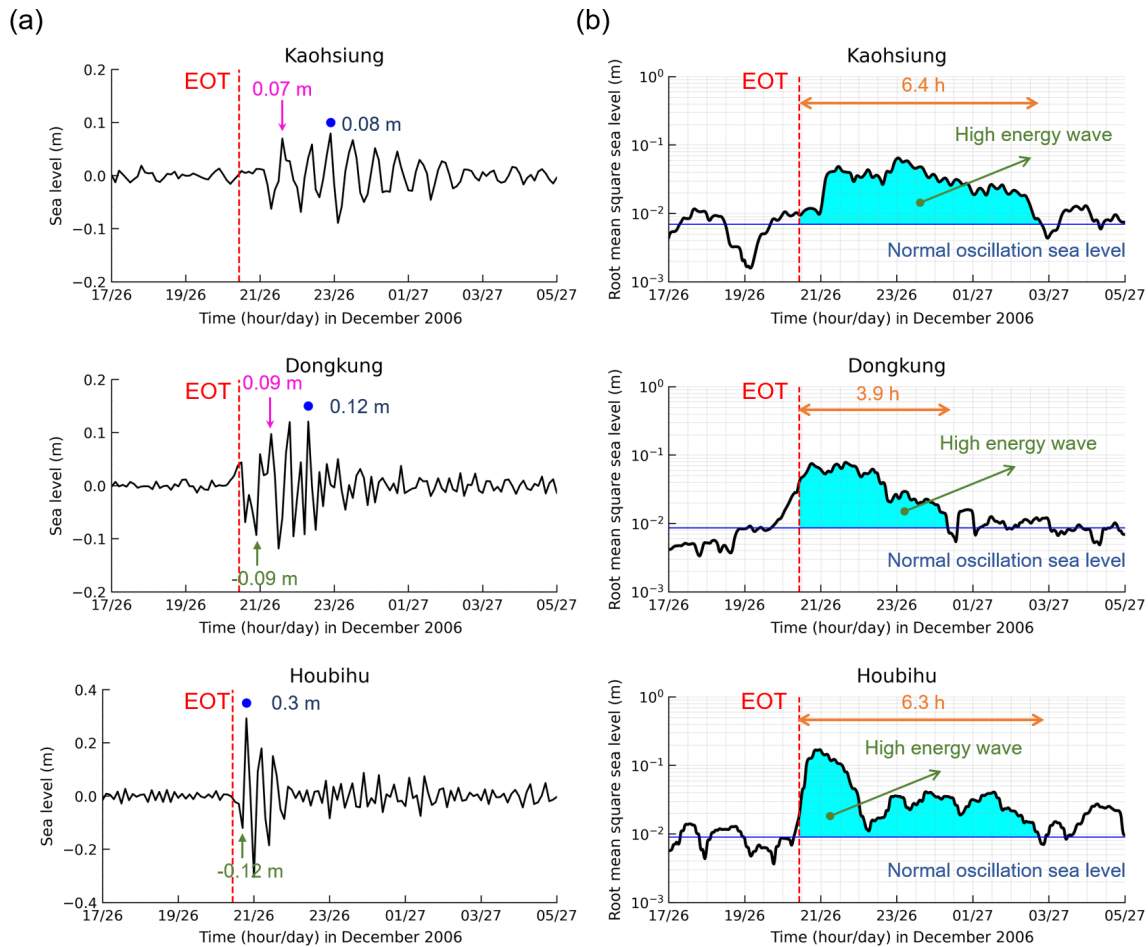


Figure 9. (a) The observed tsunami waveforms and (b) diagrams of root mean square (RMS) sea levels of the 2006 tsunami at the Kaohsiung, Dongkung, and Houbihu tide gauge stations. The vertical, dashed red lines indicate the earthquake occurrence time (EOT). The blue circles denote the arrival of the maximum crest wave that was recorded at all sites. The pink arrows mark the first wave crest. The green arrows represent the trough sign of the first wave arrival. The solid blue lines represent the normal sea level oscillation before the tsunami arrived (i.e., the mean value of sea level before the earthquake occurrence). The high-energy wave is illustrated in cyan-blue shaded areas. The orange arrows show the elapsed time of tsunami duration.

The background spectra were calculated in addition to the spectra of the observed tsunami waveform to identify the tsunami effect. The background spectra were the spectral components calculated from observed data 5 h before the tsunami’s arrival, and the spectral components of the observed tsunami waveform were computed using the 5 h of data recorded at the tide gauge after the tsunami wave arrived. Figure 10 shows the respective spectra of the observed tsunami waveform and background signals at each tide gauge station.

At all the stations, the spectral peaks of the observed tsunami spectra were estimated to be different from those of the background spectra. A visible gap also appeared in the spectral energy between the observed tsunami and the background spectra, revealing the energy generated by the arrival of tsunami waves. To examine the spectral components induced by the arrival of the tsunami waves, the spectral ratio

of the observed tsunami and background spectra was derived using Eq. (11).

$$S_T(\omega) = \frac{S_{\text{obs}}(\omega)}{S_{\text{bg}}(\omega)} \tag{11}$$

In this equation, $S_{\text{obs}}(\omega)$ is the spectral component of the observed tsunami waveform, $S_{\text{bg}}(\omega)$ is the background spectrum, and $S_T(\omega)$ is the spectral component induced by the arrival of the tsunami waves. Figure 11 shows the spectral ratios for the tsunami spectra at all the stations. Equation (11) assumes equivalent background spectra before and after the tsunami’s arrival, indicating that there was no large change in the coastal topography during the tsunami event. Although earlier studies have reported that coastal topography might be largely changed during a massive event like the 2004 Indian Ocean tsunami (Masaya et al., 2020), this was not the case for the 2006 Hengchun tsunami because the tsunami wave

Table 6. (a) Details of the tide gauge stations and physical characteristics of tsunami waveforms during the 2006 tsunami. (b) Details of the tide gauge stations and physical characteristics of tsunami waveforms during the 2006 tsunami.

(a)					
Station	Longitude (° E)	Latitude (° N)	Tsunami wave amplitude (m)		
			First trough sign	First wave crest	Maximum wave crest
Kaohsiung	120.28	22.61	−0.06	0.07	0.08
Dongkung	120.43	22.46	−0.09	0.09	0.12
Houbihu	120.74	21.94	−0.12	0.3	0.3

(b)					
Station	Arrival time (national standard time)			Delay of maximum wave crest (min)	Visible wave period (min)
	First trough sign	First wave crest	Maximum wave crest		
Kaohsiung	21:18	21:44	22:54	70	30–48
Dongkung	20:54	21:18	22:18	60	18–24
Houbihu	20:42	20:48	20:48	0	18–24

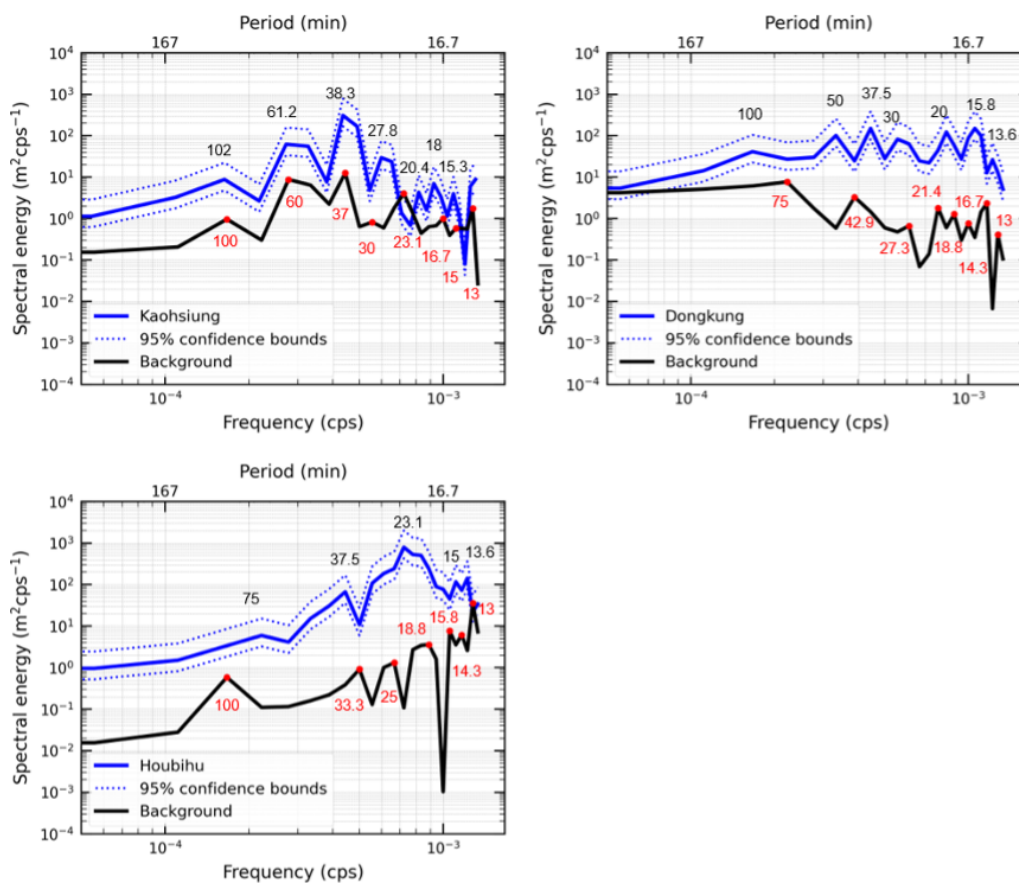


Figure 10. Respective spectra of the observed tsunami waveform (solid blue lines) at each tide gauge station. The solid black lines are spectra for the background signals before tsunami arrivals at each station. The red circles denote the dominant periods of the background spectra.

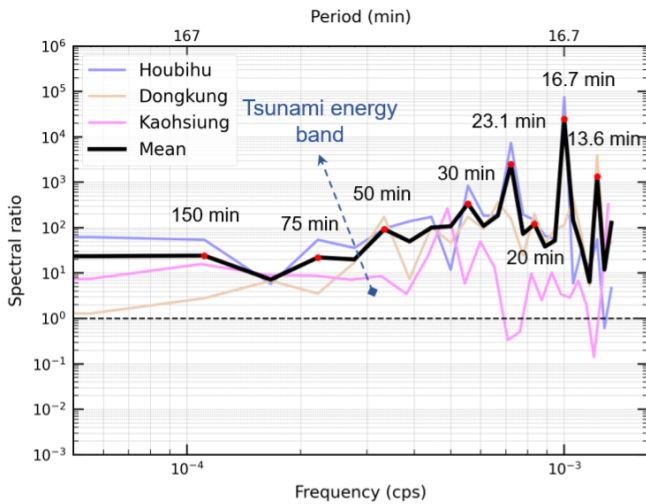


Figure 11. Respective spectral ratios for the tide gauge spectra. The solid black line is the calculated mean spectral ratio of the three tide gauge spectra. The red circles represent the dominant periods of the mean spectral ratio.

was small. Therefore, the dominant peaks of the spectral ratio were connected to either the tsunami source or perhaps the wave oscillation induced by the non-source phenomenon.

Tsunami source periods are periodic components that primarily appear in coastal observations close to the tsunami source region (Rabinovich, 1997). Accordingly, the tsunami source periods can be estimated from the mean of the spectral ratios calculated from all three stations (i.e., the solid black line shown in Fig. 11). From the analysis result of the spectral ratio, the periods of 13.6, 16.7, and 23.1 min are distinct in comparison to other periodic components. The periods within this band most likely presented the source periods of the 2006 tsunami since the periodic components within this band were mostly visible at all stations.

In general, a larger earthquake can ordinarily generate a larger tsunami wave with a longer period. For instance, the major periods of the 2011 Tohoku-Oki earthquake tsunami were reported to be 37–67 min associated with that magnitude M_w 9.0 earthquake (Heidarzadeh and Satake, 2013), while shorter dominant periods of 10–22 min were found for the 2013 Santa Cruz tsunami, a M_w 8.0 earthquake (Heidarzadeh and Gusman, 2021). According to Rabinovich’s theory (Rabinovich, 1997), the approximate dimensions of the fault rupture can be estimated from the source periods using the empirical formula defined in Eq. (12):

$$L = \frac{T}{2} \sqrt{gh}, \quad (12)$$

where g stands for the gravitational acceleration and is set to a constant value of 9.81 m s^{-2} , h represents the seafloor depth around the tsunami source region, L denotes the fault rupture dimensions of length or width, and T is the source period. The approximate source region could be illustrated

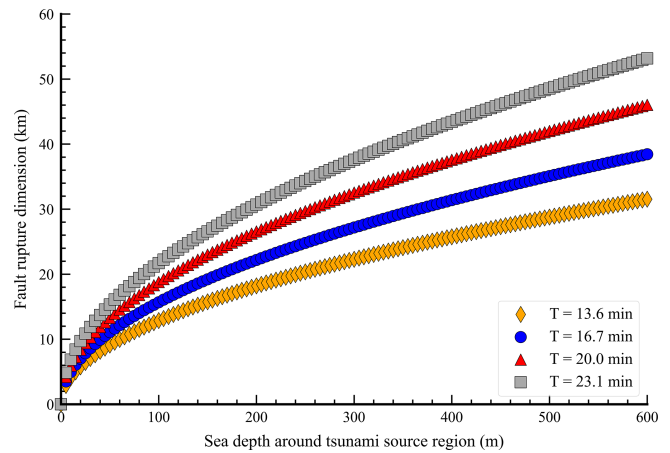


Figure 12. Correlation of earthquake fault dimensions and sea depth around the tsunami source region derived from the empirical formula proposed by Rabinovich (1997).

based on the aftershock distribution 1 d after the first earthquake occurred. Assuming that the sea depths around the tsunami source region range from 0–600 m and the source periods are 13.6, 16.7, 20.0, and 23.1 min, the relationship between the fault rupture dimensions and sea depths can be derived from Eq. (12). The correlation derived from Eq. (12) is plotted in Fig. 12.

Assuming that the mean sea depth around the tsunami source region is 300 m, the fault rupture dimensions for the two earthquakes can be estimated to be 20–40 km. The approximate fault size of these two earthquakes was estimated to be 800 km^2 , for which a longer dimension of 40 km was considered the fault length and 20 km was considered the fault width. The estimation of fault size was fairly consistent with the results derived from the empirical scaling relations of Papazachos et al. (2004), with a fault area of 794 km^2 associated with the M_w 7.0 normal fault earthquake (first earthquake) and 738 km^2 associated with the M_w 6.9 strike-slip fault (second earthquake).

4.2 Resonance modes induced by tsunami trapping waves

In addition to the Fourier analyses, wavelet (time–frequency) analyses were also applied to 15 h of de-tided observed data (i.e., from 15:00 on 26 December 2006 to 06:00 on 27 December 2006, national standard time) at all the stations. Wavelet analyses are commonly employed as a method to examine periodic variations over time series through the distribution of tsunami spectral energy. Figure 13 shows the tsunami wavelets derived from the tsunami records observed at each station. According to the wavelet plots at all the stations, period bands of 13.6–23.1 min were clearly recorded after the first wave arrived at all the stations. This also confirmed that the period bands of 13.6–23.1 min were associ-

ated with the source periods. At Kaohsiung, the tsunami energy became apparent with periods of 16 and 36 min approximately 3 h after the arrival of the first wave. In the period channel of 16 min, the oscillation was preserved for approximately 5 h, while the 36 min channel was occupied by a high-energy wave for more than 9 h. At Houbihu, more energy was channeled than at other stations in the period bands of 13.6–23.1 min soon after the first earthquake. This was reasonable because Houbihu was the closest station to the epicentral region and was therefore considered to be more sensitive to the tsunami source than the other stations were. Following the arrival of the first wave, the persistent oscillation (i.e., lasting more than 4 h) was visible approximately 2 h after the first earthquake in the period channels of 16, 16.4, 20, 22.5, 25.7, 30, 36, and 60 min. These periodic components were considered as possible modes of trapped tsunami waves resonating within the shelf since the wave resonance commonly requires some time to be formed (Heidarzadeh et al., 2021). Among these periods, the 16 and 36 min periods most likely presented the resonance mode since that mode is visible at only the Kaohsiung and Houbihu stations, where tsunami durations of more than 6 h were recorded (Fig. 9b). From the wavelet analysis of the observed data recorded at the tide gauge stations, the persisting wave oscillations at the Kaohsiung and Houbihu stations might be attributed to tsunami resonance.

5 Sensitivity analyses of source models and bathymetry data

5.1 Single fault models

5.1.1 Tsunami sensitivity to fault depths

The sensitivity of simulated tsunami waveforms to fault depth was evaluated by varying the central fault depths of the first earthquake. Fault dimensions of 40 km × 20 km were applied to the two earthquakes. The single fault model of the two earthquakes was constructed using the GCMT solution of nodal plane NP2 for the first earthquake and NP1 for the second earthquake. The tide gauge stations of Dongkung and Houbihu were chosen for this sensitivity analysis because they were the closest stations to the source region and were therefore more sensitive to the tsunami source. The single fault models of the two earthquakes and the locations of the near-field tide gauge stations that were used for the sensitivity analysis of fault depths are shown in Fig. 14a.

Figure 14b shows the observed and simulated tsunami waveforms at the Dongkung and Houbihu stations using different fault depths of the first earthquake. At the Dongkung station, the first circle of simulated tsunami waveforms matched the observed data well regardless of the fault depths. At the Houbihu station, the first wave crest of the simulated waveform from a fault depth of 35 km was half the size of

the observed value. Simulated tsunami waveforms with shallower depths of 15 and 20 km produced significantly higher amplitudes during the arrival of the first crest wave. These results revealed that coastal sites with a shorter distance to the source are more sensitive to earthquake fault depths. The simulated waveforms from a central fault depth of 20 km fit the observed data better than other simulations did, and therefore, this was considered the best fault depth for simulation.

5.1.2 Comparison of eight models

Single fault models with fault dimensions of 40 km × 20 km and central depths of 20 km for the first earthquake and 33 km for the second earthquake were used in tsunami simulations using eight different sets of focal mechanisms for the two earthquakes estimated from GCMT and USGS data. The single fault models of the two earthquakes with different focal mechanisms are plotted in Figs. 15 and 16. The details of the eight different sets of earthquake focal mechanisms are listed in Table 7.

In general, the simulated tsunami waveforms from all eight sets of earthquake focal mechanisms matched the observed data well. Figure 17 shows the observed and simulated tsunami waveforms at the Dongkung and Houbihu stations using the eight different sets of earthquake focal mechanisms. The simulated tsunami waveform from the earthquake focal mechanisms of S3 (misfit = 0.530), S5 (misfit = 0.529), and S7 (misfit = 0.493) showed a better fit to the observations than the other simulations did (Table 7). Among them, the earthquake focal mechanisms of S7 were found to be the best fitting scenario with the smallest misfit from the observations. Scenario S7 contained the fault orientations of NP2 for the first earthquake and NP1 for the second earthquake from USGS's moment tensor solution (Figs. 15d, 16c).

While the single fault models can produce simulated tsunami waveforms that are consistent with the observations, the poorly sampled (i.e., 6 min interval) signals recorded at the coastal stations also raised some questions, as one would expect some potential high tsunami waves behind the observed signals. To that sense, overestimation of the modeled results was expected, but the simulated tsunami waveforms using single fault models presented the opposite results. This indicates that the single fault models (i.e., with uniform fault slip) may not be sufficient and that the asperity area (i.e., with a large fault slip) on the fault should be evaluated. The tsunami sensitivity to asperity locations of multiple fault models is discussed in the next section.

5.2 Tsunami sensitivity to uniform and non-uniform fault slip models

The sensitivity of simulated tsunami waveforms to non-uniform fault slip distribution was evaluated based on the best fitting fault geometry of S7. The fault model with uniform slip was also modeled to identify the significant dif-

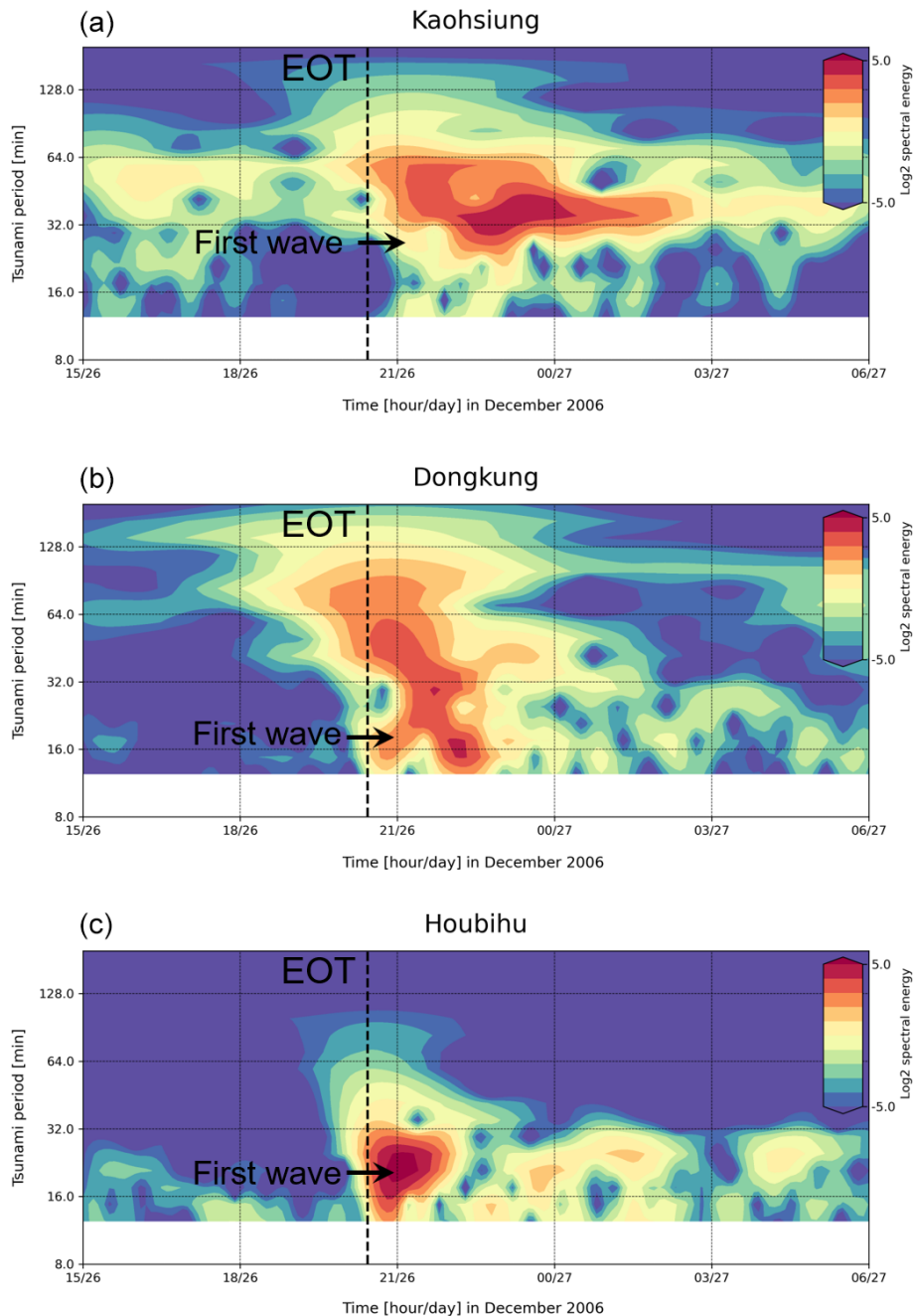


Figure 13. Wavelet (time–frequency) diagrams of tsunami data for the 26 December 2006 tsunami event at the (a) Kaohsiung, (b) Dongkung, and (c) Houbihu tide gauge stations. The color map represents the \log_2 spectral energy at various times and tsunami periods. The vertical, dashed black lines indicate the earthquake occurrence time (EOT). The black arrows denote the arrival time of the first tsunami wave at each station.

ferences in the modeled results from the uniform and non-uniform slip fault models.

Figure 18 shows the observed and simulated tsunami waveforms at the Dongkung and Houbihu stations using non-uniform slip models (nine cases in total) and a uniform slip model. At the Houbihu station, the simulated tsunami waveforms from multiple fault models were not much differ-

ent from those of the single fault models. Both models could produce tsunami waveforms in good agreement with the observed values recorded at this station. At the Houbihu station, the non-uniform slip models produced a significantly higher first wave crest than the observations. The simulated wave peaks from the non-uniform slip models produced wave heights approximately twice those simulated using the uni-

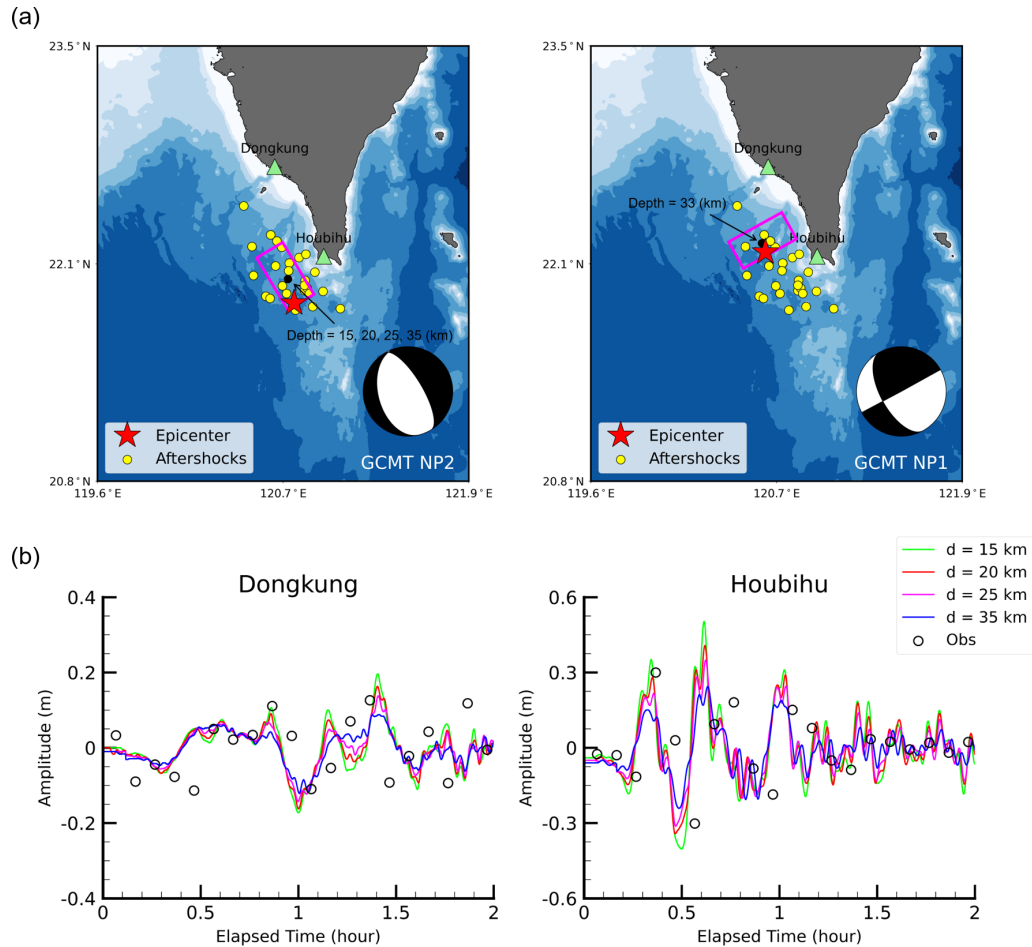


Figure 14. (a) Single fault models with fault dimensions (length \times width) of $40 \text{ km} \times 20 \text{ km}$ of the first earthquake using the GCMT NP2 nodal plane and the second earthquake using the GCMT NP1 nodal plane. The central fault depths of the single fault models for the first earthquake are set as 15, 20, 25, and 35 km, and the central fault depth is fixed at 33 km for the single fault models of the second earthquake for the tsunami sensitivity test. (b) Observed and simulated tsunami waveforms at the Dongkung and Houbihu stations using single fault models with the different central fault depths of the first earthquake.

Table 7. Validation of the simulated tsunami waveforms using single fault models with eight different models of focal mechanisms estimated by GCMT and USGS.

Scenario	Moment tensor solution	Nodal plane		Misfit of simulated tsunami waveforms
		Earthquake 1	Earthquake 2	
S1	GCMT	NP1	NP1	0.591
S2		NP1	NP2	0.632
S3		NP2	NP1	0.530
S4		NP2	NP2	0.661
S5	USGS	NP1	NP1	0.529
S6		NP1	NP2	0.604
S7		NP2	NP1	0.493
S8		NP2	NP2	0.735

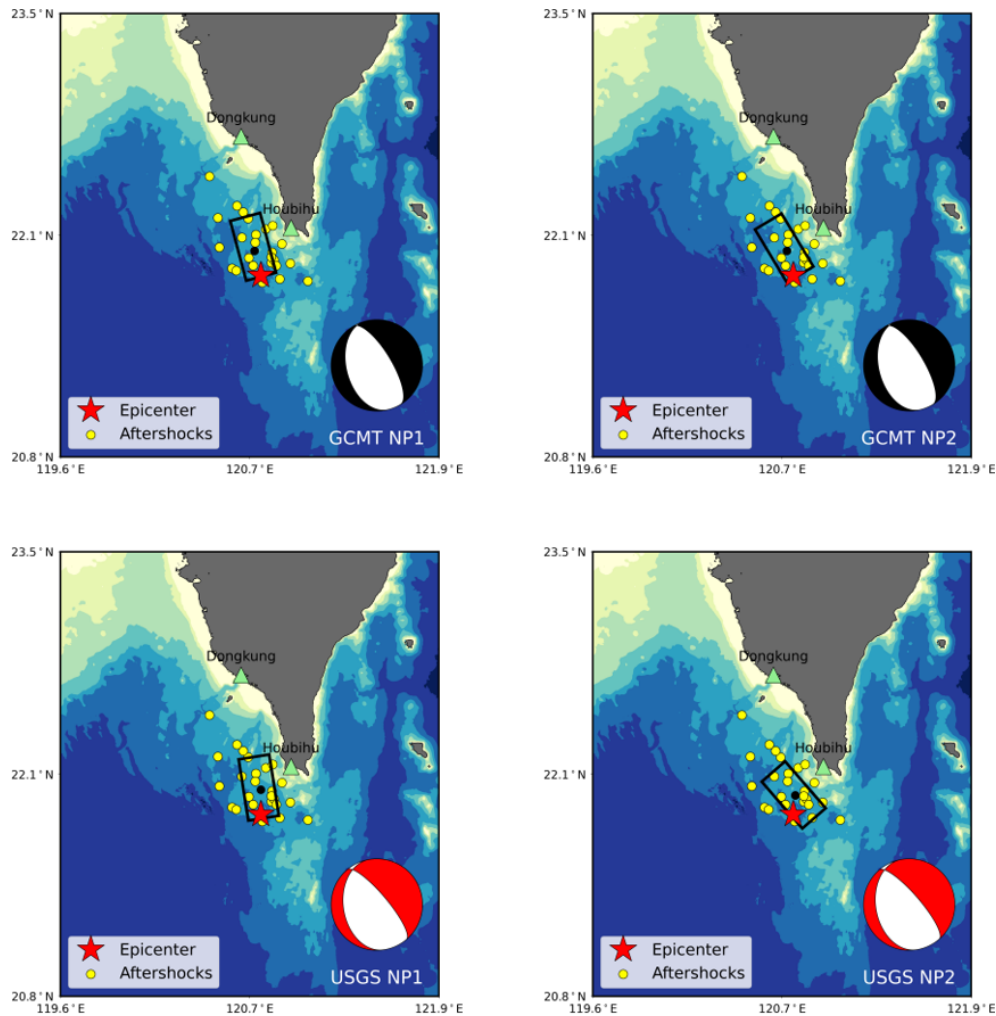


Figure 15. Simple fault models of the first earthquake (M_w 7.0) using the focal mechanisms from GCMT and USGS. The green triangles indicate the tide gauge stations, red stars indicate the epicenter, yellow circles indicate aftershocks, and the black rectangles indicate the fault model.

form slip. These results indicated that the near-field station of Houbihu was rather sensitive to the effect of the fault slip distribution, and some high tsunami waves might have been missing from the recorded signals at the Houbihu station during the 2006 tsunami.

5.3 Tsunami simulation using open-source bathymetric data

To analyze the tsunami sensitivity to different sources of open-source, accessible bathymetry data, numerical simulations were applied using GEBCO and ETOPO1 data. The differences between the modeled results using these different bathymetry data were evaluated to compare the modeled wave peaks and waveforms of the 2006 tsunami.

Figure 19a and b show the spatial distribution of the maximum wave heights simulated using two bathymetric grids, the GEBCO data and ETOPO1 data. To evaluate the differ-

ences between the modeled wave peaks, the variation and percent change in the variation were calculated, which can be defined in Eqs. (13) and (14):

$$\text{Var}_{\text{peak}} = \text{Peak}_{\text{GEBCO}} - \text{Peak}_{\text{ETOPO1}}, \quad (13)$$

$$\% \text{Var}_{\text{peak}} = \frac{\text{Peak}_{\text{GEBCO}} - \text{Peak}_{\text{ETOPO1}}}{\text{Peak}_{\text{GEBCO}}} \times 100, \quad (14)$$

where Var_{peak} is the variation in the modeled wave peaks calculated at each computational grid with GEBCO and ETOPO1 data, and $\text{Peak}_{\text{GEBCO}}$ and $\text{Peak}_{\text{ETOPO1}}$ are defined as the calculated wave peaks of progressive waves in a unit area of the free surface. Figure 19c and d illustrate the spatial distribution of the variation and percent change in the variation of the modeled wave peaks in the model domain, indicating the differences in the modeled results using the two bathymetries. The results suggested that the variation in the modeled wave peaks using the two bathymetries was greater

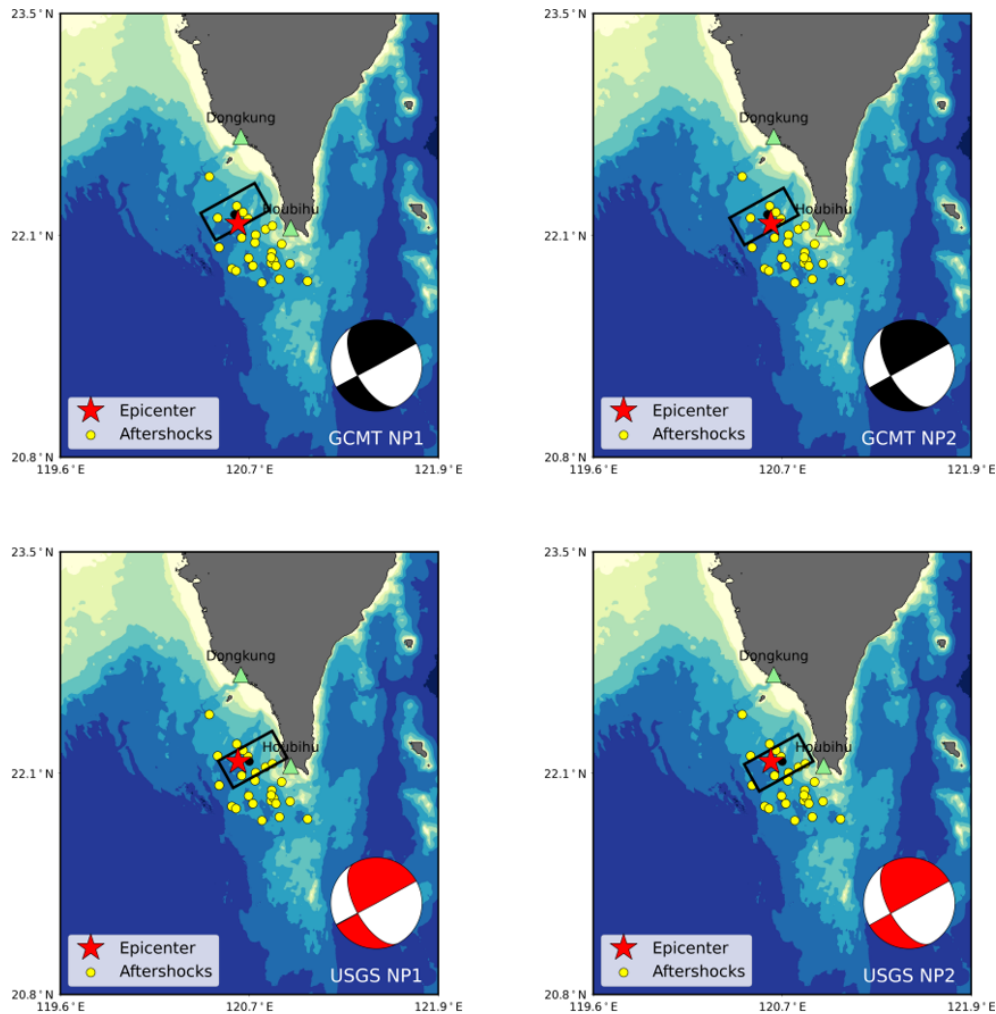


Figure 16. Simple fault models of the second earthquake (M_w 6.9) using the focal mechanisms from GCMT and USGS. The green triangles indicate the tide gauge stations, red stars indicate the epicenter, yellow circles indicate aftershocks, and the black rectangles indicate the fault model.

than 0.05 m and that the percent change was greater than 50 % between the modeled results for areas with sea depths of less than 500 m.

Figure 20 shows the modeled tsunami waveforms at the three coastal stations (i.e., black circles in Fig. 19) using the two bathymetric grids. At Kaohsiung, the modeled waveforms from the two bathymetries matched each other well; however, the modeled wave peak from the ETOPO1 data was significantly smaller than that from the GEBCO data. The bathymetries from the GEBCO and ETOPO1 data could produce tsunami waveforms at Dongkung and Houbihu that were similar in both wave periods and peaks. Table 8 summarizes the details of the coastal stations and the peak variation percentage of the modeled results from the two bathymetries.

6 The mechanism of tsunami wave trapping

6.1 Bathymetry effect on tsunami wave directivity

It is commonly understood that tsunami velocities are mainly governed by seafloor depths. A tsunami propagates at a slower speed when the tsunami wave enters shallow water from deeper water. The significant change in propagation speed allows the tsunami to change its wave direction. To assess the bathymetry effect on tsunami wave directivity during propagation, simulations were applied using actual (MS) and manipulated bathymetry experiments (EXP1 and EXP2).

Simulated snapshots of tsunami wave propagation using actual (MS) bathymetry data are shown in Fig. 21. The continental shelves in front of Hengchun Peninsula have shallow depths compared to the open ocean. Figure 21a and b present how tsunami waves repeatedly changed their directions among the shelves and then refracted into the west

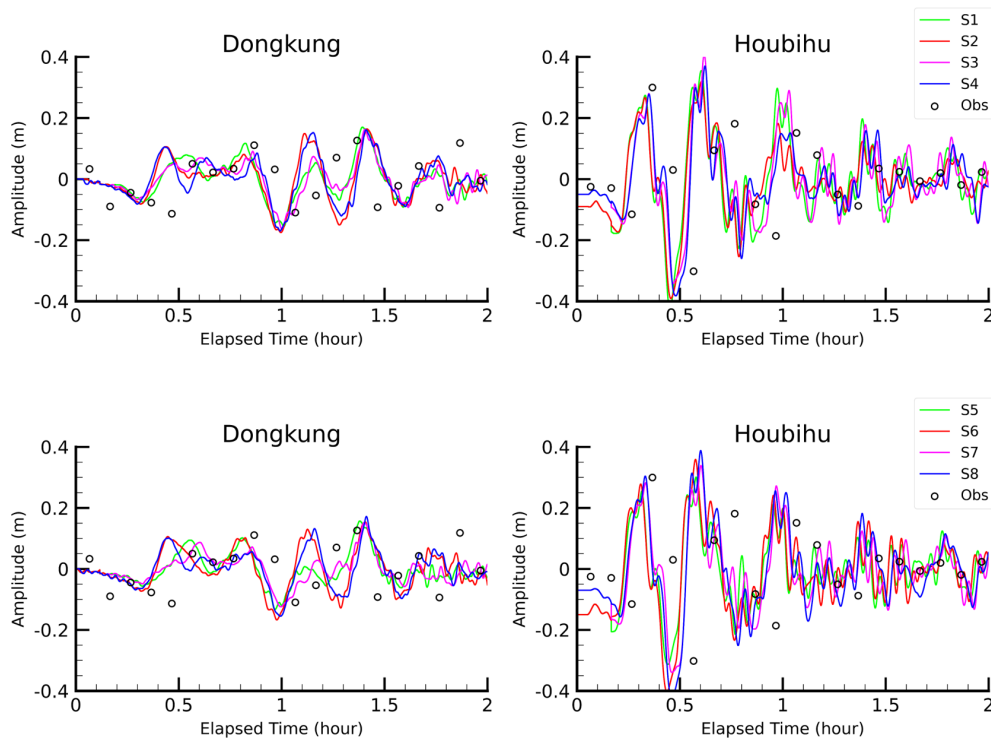


Figure 17. Comparison of simulated tsunami waveforms at the Dongkung and Houbihu stations using single fault models with eight different models of focal mechanisms estimated by GCMT and USGS.

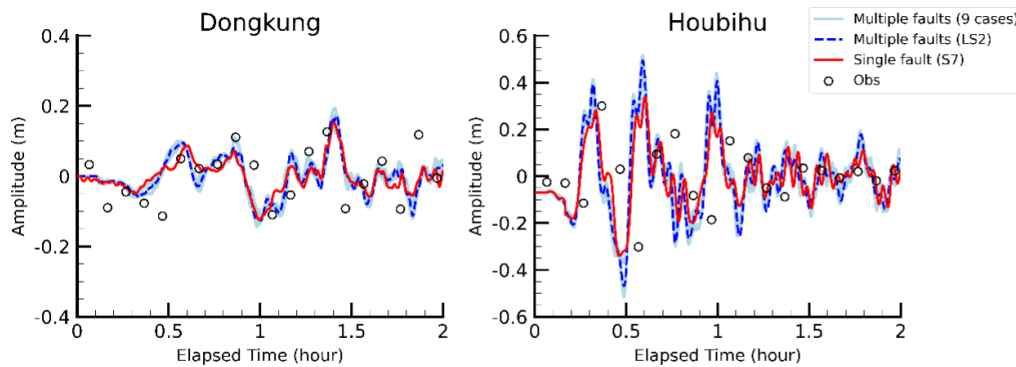


Figure 18. Comparison of simulated tsunami waveforms at the Dongkung and Houbihu stations using nine cases of multiple fault models (solid blue lines) and a single fault model of S7 (solid red lines). The simulated tsunami waveforms using the multiple fault model (LS2) are shown as dashed blue lines. The white circles represent the observational data.

Table 8. Details of the locations of the simulated tsunami waveforms and misfit of model results using different open-source bathymetry data at three tide gauge stations.

Station	Sea depth (m)		Simulated wave peak (m)		Var _{peak}	%Var _{peak}
	GEBCO	ETOPO1	GEBCO	ETOPO1		
Kaohsiung	10	8	0.163	0.084	0.079	48.45
Dongkung	9	14	0.171	0.17	0.001	0.58
Houbihu	4	11	0.493	0.414	0.079	16.02

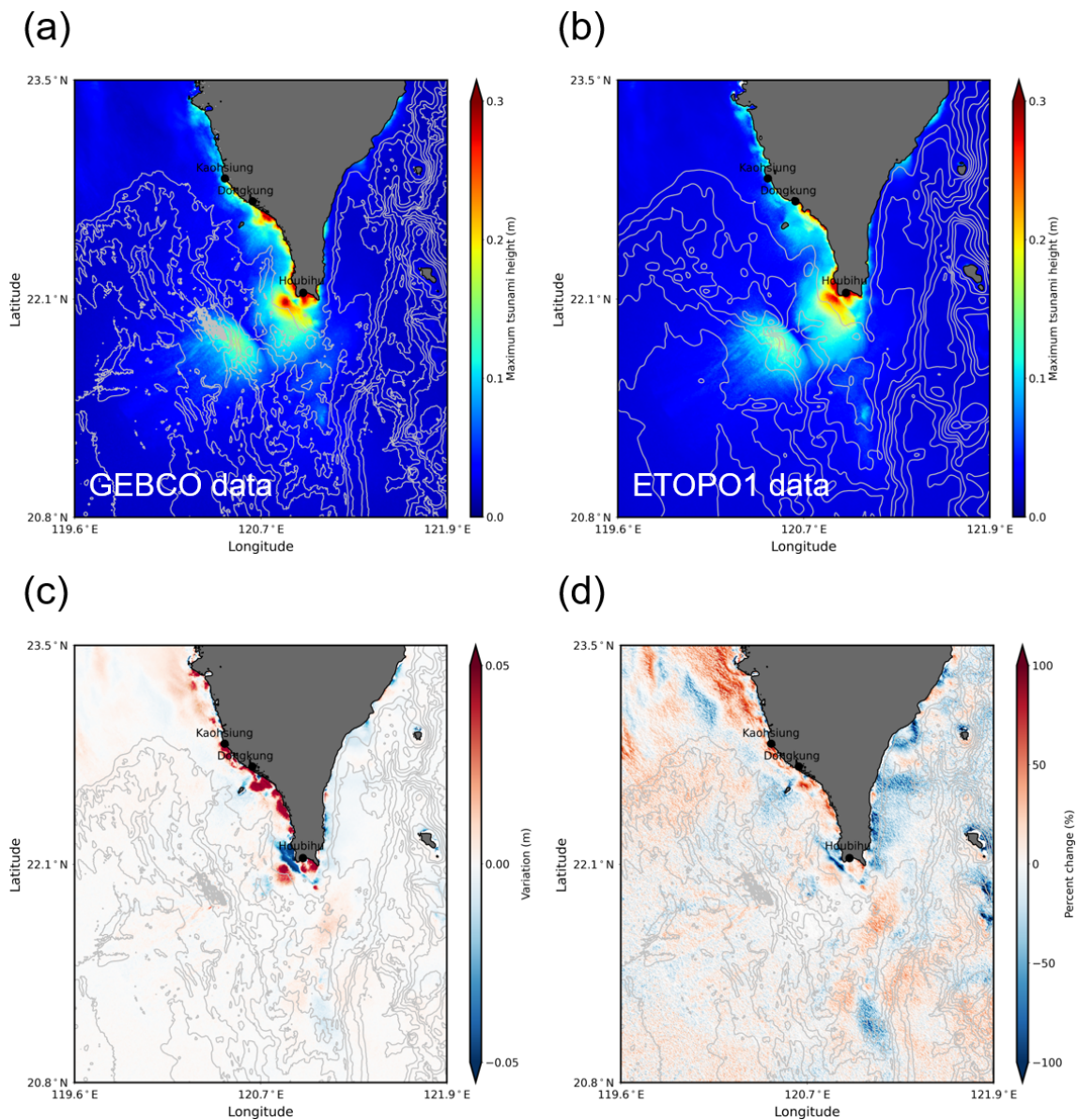


Figure 19. Simulated maximum tsunami height using open-source bathymetry data: (a) GEBCO and (b) ETOPO1 data. (c) The variation and (d) the percent variation in the simulated maximum tsunami height using two sources of bathymetry data. The black circles indicate the locations of the tide gauge stations. The bathymetry contour is 500 m based on the GEBCO or ETOPO1 bathymetric data.

coast embayment. The tsunami waves were reflected from the coast after arrival and tended to radiate offshore. However, they did not fully radiate offshore; instead, they were reflected again at the boundary of the shelf and refracted north toward Kaohsiung and Dongkung (Fig. 21c, d). The high-energy waves repeatedly reflected and refracted among the shelves. Only rarely were tsunamis transmitted back to the open ocean or to the east coast. These results indicated that the tsunami waves were trapped over the shelves during their passage in the 2006 tsunami event. Due to this fluctuation, the high-energy tsunami wave remained along the western coast for a long time, which could be clearly seen at 75 and

90 min after the occurrence of the first earthquake (Fig. 21e, f).

Figure 22 shows snapshots of the simulated tsunami wave propagation using manipulated (EXP1) bathymetry. In this situation, the transmission of tsunami waves in the shallow area was similar to those simulated using the actual (MS) bathymetry, in which the tsunami waves were persistent and repeatedly reflected and refracted among the shelves, but more reflected waves from the coast radiated to the open sea (Fig. 22b–f). This is because the tsunami source was located in an area with sea depths over 500 m, and bathymetry data

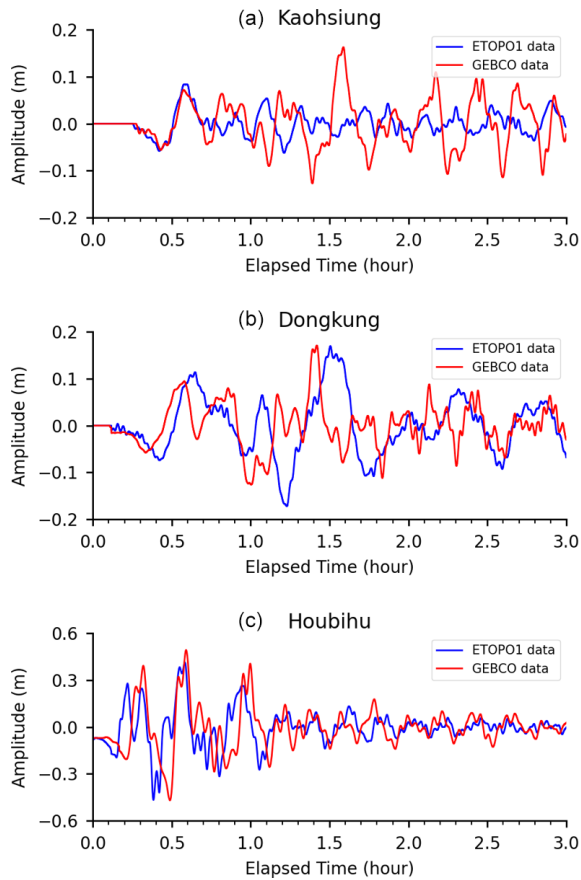


Figure 20. Simulated tsunami waveforms at the (a) Kaohsiung, (b) Dongkung, and (c) Houbihu stations using two different open-source bathymetry datasets, GEBCO and ETOPO1.

with sea depths over 500 m were replaced with a 500 m depth in this hypothetical situation.

Aside from the numerical experiment EXP1, a rather hypothetical situation (EXP2) was conducted to simulate tsunami wave propagation on a bathymetry with a flat sea bottom and a sea depth of 500 m. Figure 23 shows snapshots of simulated tsunami wave propagation using the manipulated (EXP2) bathymetry. An inspection of the tsunami wave transmission in the shallow area indicated that the reflected tsunami waves from the coast radiated homogeneously offshore, and the wave reflection and refraction could not be clearly seen. In addition, the tsunami waves propagated at a rather fast speed (i.e., in comparison to MS and EXP1) and mostly radiated out of the model domain at 75 and 90 min after the occurrence of the first earthquake (Fig. 23d, e).

6.2 Tsunami wave energy trapped on the shelf

While the past section specified that tsunami waves are trapped over shelves due to the wave directivity change associated with the configuration of coastal bathymetry, the question remains of how much wave energy can be trapped over

the shelves in front of southern Taiwan during the passage of tsunamis. To quantitatively evaluate the wave energy trapped over the shelves, the trapped ratio was used to indicate the tsunami energy trapped in bathymetric situations, as calculated in Eq. (15):

$$R_T = \frac{E_{\text{Shelf}}}{E_{\text{Total}}} \times 100, \quad (15)$$

where R_T is the ratio of tsunami energy trapped, E_{Shelf} is the calculated tsunami potential energy on the shelves (i.e., shallow areas with sea depths under 500 m), and E_{Total} is the calculated total tsunami potential energy of the model domain at each time step. The tsunami potential energy was determined assuming that the energy flux of the tsunami wave progressed in a unit region of the free sea surface and was determined using Eq. (16) (Nosov et al., 2014):

$$E_p = \iint \frac{1}{2} \rho g \eta^2 dx dy, \quad (16)$$

where E_p is the tsunami potential energy, ρ is the water density of the ocean, g is the gravitational acceleration (set as 9.81 m s^{-2}), and η represents the surface integral of the ocean surface disturbance at each time step. The ratio of trapped tsunami energy was calculated from the snapshots of tsunami simulations using actual (MS) and manipulated (EXP1 and EXP2) bathymetry. Figure 24 shows the calculated trapped ratio from simulated tsunami propagation snapshots every 15 min using actual (MS) and manipulated (EXP1 and EXP2) bathymetry. Note that for calculating the trapped ratio from simulations using manipulated bathymetry (EXP1 and EXP2), the shelf region corresponding to the actual bathymetry (MS) was used (i.e., the shallow area illustrated by the solid and dashed black lines shown in Figs. 22 and 23). According to Eqs. (15) and (16), the simulations yielded a ratio of trapped tsunami energy of more than 50 % when using actual bathymetry (MS) and manipulated bathymetry (EXP1) but a smaller trapped ratio of 20 % when using manipulated bathymetry (EXP2). These results quantitatively provided another confirmation that the coastally trapped tsunami wave energy was related to the shape of the bathymetry.

6.3 Comparison of simulated tsunami waveforms

To understand any significant change in tsunami waveforms that can be recognized with and without wave trapping, tsunami waveforms simulated from actual (MS) and manipulated bathymetry (EXP1 and EXP2) were compared. Figure 25 shows the simulated tsunami waveforms at the three coastal stations in southern Taiwan using actual and manipulated bathymetry.

Using the manipulated bathymetry (EXP1), the first few circles of simulated tsunami waveforms at all the stations were consistent with those simulated using actual bathymetry (MS) but produced slightly smaller later-phase amplitudes.

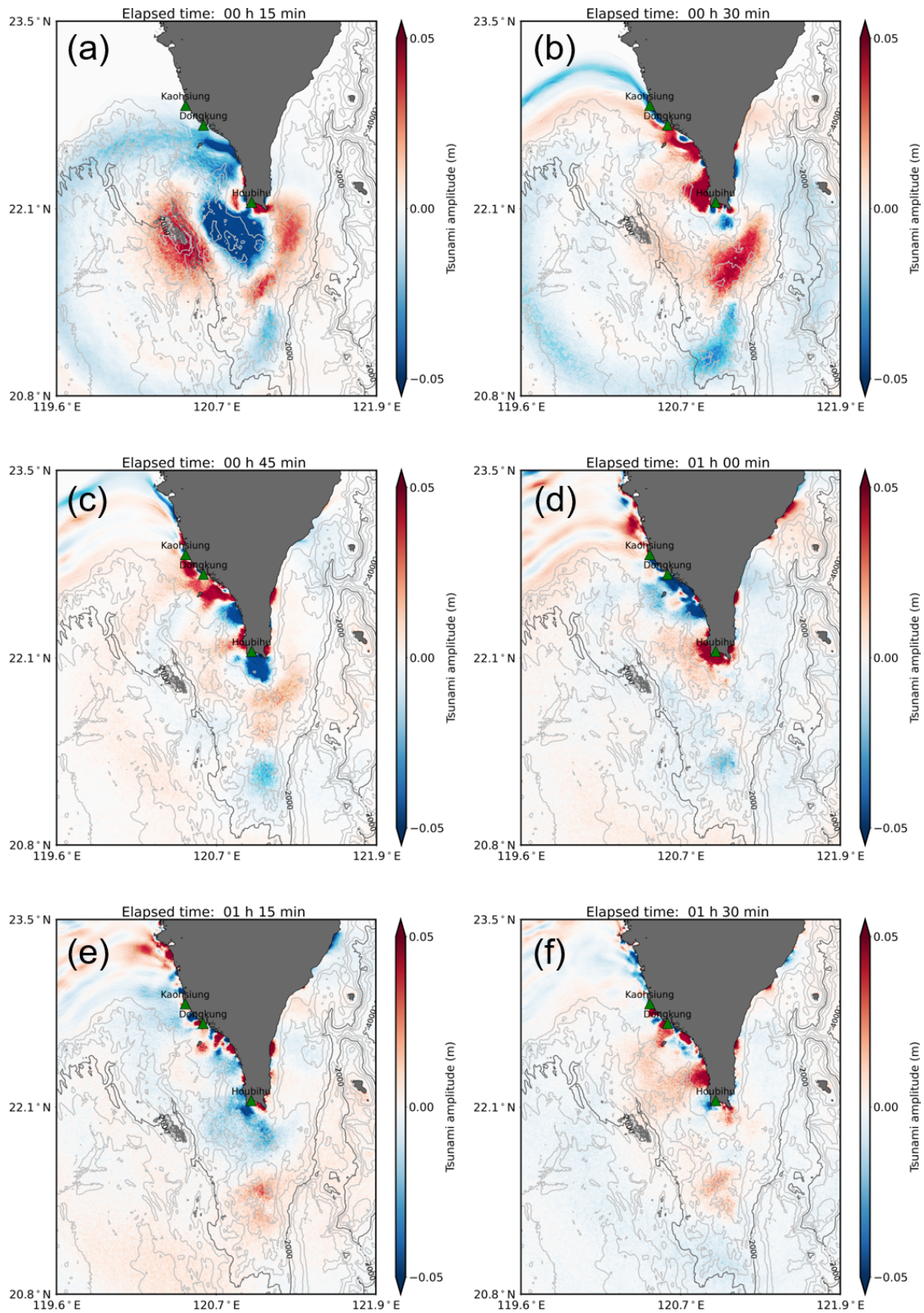


Figure 21. Tsunami propagation snapshots from the numerical experiment MS. The tide gauge stations are plotted in green triangles. The bathymetry contour is 500 m.

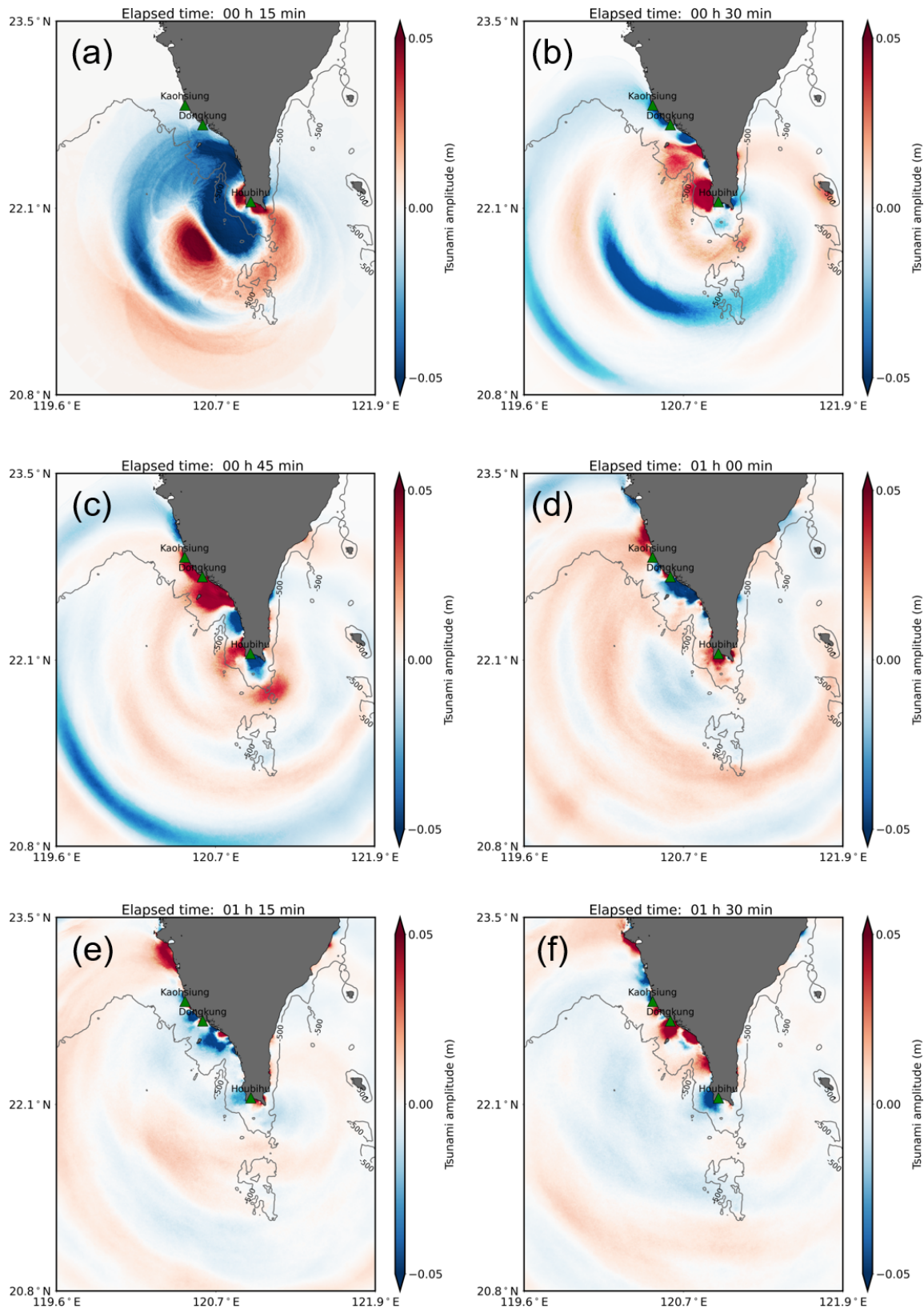


Figure 22. Tsunami propagation snapshots from the numerical experiment EXP1. The tide gauge stations are plotted as green triangles. The bathymetry contour at a depth of 500 m is shown as a solid gray line.

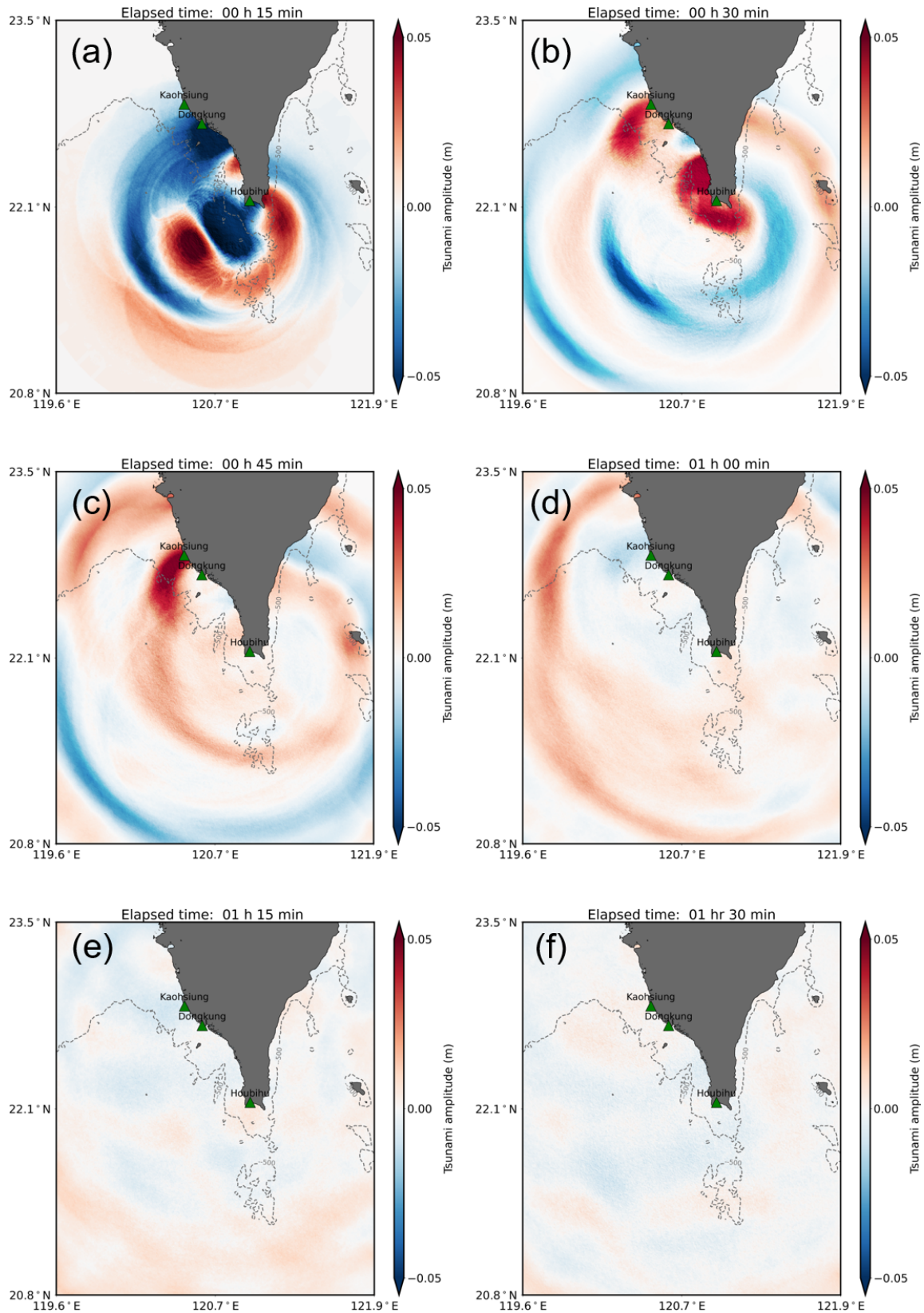


Figure 23. Tsunami propagation snapshots from the numerical experiment EXP2. The tide gauge stations are plotted as green triangles. The corresponding bathymetry contour of 500 m depth from GEBCO data is shown as a dashed gray line.

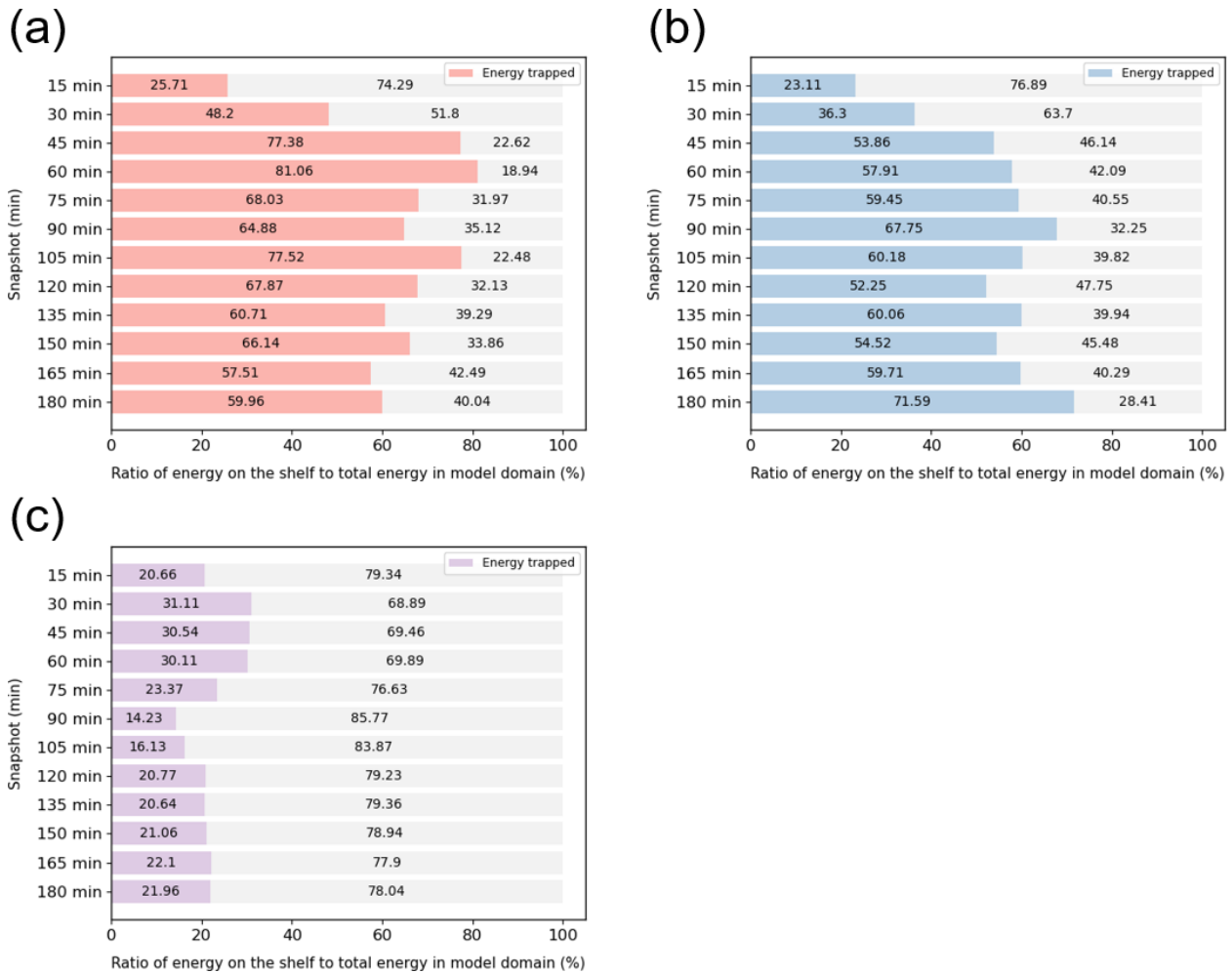


Figure 24. Trapped ratio calculated from tsunami propagation snapshots every 15 min from numerical experiments (a) MS, (b) EXP1, and (c) EXP2.

An inspection of the simulated waveforms using the manipulated bathymetry (EXP2) indicated an earlier arrival time of the first wave and smaller amplitudes of the later phase than those of the simulation results using actual (MS) bathymetry. These results indicated that the persistent high-energy waves along the south coast of Taiwan were associated with the mechanism of tsunami wave trapping.

6.4 Amplified and persistent high-energy waves along the coast

As described in the previous sections, the tsunami wave was trapped over the shelves and transmitted along the coast as edge waves during the 2006 tsunami. This section describes how tsunami waves behave as edge waves and to what extent such wave fluctuations influence the amplified and persisting high-energy waves along the south coast of Taiwan. Figure 26 shows the shelves in front of south Taiwan and the

simulated tsunami heights of the 2006 tsunami from the main simulation (MS).

To study the behaviors of edge waves along the south coast during the 2006 tsunami, a time–distance diagram of tsunami waves is shown. Figure 27a shows the time–distance diagram of the tsunami wave along the contour of the 20 m sea depth (i.e., dashed black line in Fig. 26a). Based on the phase shift of the tsunami wave, the propagation path and the travel time curve of edge waves are illustrated (i.e., green arrow in Fig. 27a). According to the travel time curve, the edge waves propagated along the coast at a speed of 50 m s^{-1} . The edge waves propagated along the coast and were iteratively reflected at the shelf edge. The coupling of the edge waves and the later-arriving incident waves amplified the tsunami waves and maintained the wave oscillation in the later phase. These were visible from simulated tsunami waveforms at numerical wave gauges C and E, as shown in Fig. 27c.

To understand the persisting high-energy waves along the south coast of Taiwan during the 2006 tsunami, the decreas-

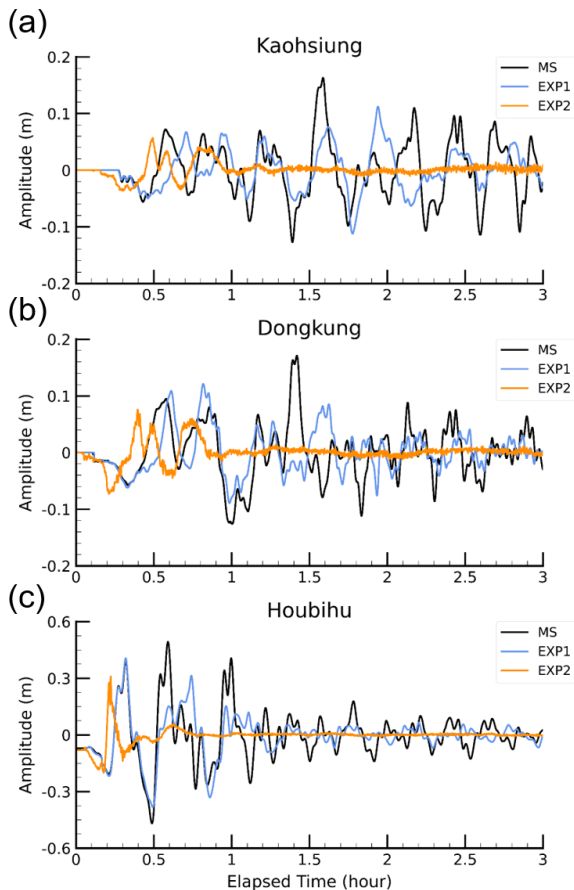


Figure 25. Simulated tsunami waveforms at the (a) Kaohsiung, (b) Dongkung, and (c) Houbihu stations from numerical experiments MS, EXP1, and EXP2.

ing tendency of the tsunami wave energy along the 20 m sea depth contour was analyzed. The temporal tsunami wave energy was first determined using Eq. (16) and then normalized according to the maximum temporal tsunami energy in the time series. Figure 27b shows the time–distance diagram of the normalized tsunami energy along the 20 m sea depth contour (i.e., dashed black line in Fig. 26a). Figure 27d shows the normalized tsunami energy at numerical wave gauges C and E. At the numerical wave gauge C, the normalized tsunami energy achieved its greatest value at approximately 40 min after the first earthquake occurred. However, this high-energy channel did not decrease with time after the first wave arrived; instead, a persisting channel of strong energy was visible. This energy channel lasted for more than 60 min, and the wave energy repeatedly reached the maximum value in this channel. Beyond this channel, the energy commenced to decrease with a rate of energy loss of 50 % at 110 min and 20 % at 270 min after the occurrence time of the first earthquake. At the numerical wave gauge E, the normalized tsunami energy achieved its greatest value approximately 30 and 120 min after the first wave arrived. Beyond this chan-

nel, the energy commenced to decrease at a rather fast rate of energy loss of 80 % at 150 min and 70 % at 215 min after the occurrence time of the first earthquake. Accordingly, the tsunami decay process in this region was expected to last for more than 300 min. These results indicated that the wave amplification and persistent high-energy waves along the coast during the 2006 tsunami were connected to tsunami wave trapping and the influence of edge waves. According to these behaviors, southern Taiwan could be affected by intensified coastal hazards and severe impacts from tsunamis.

7 Conclusions

7.1 Main findings

In this article, the characteristics of the consecutive tsunamis on 26 December 2006 and the resulting tsunami behaviors in southern Taiwan were investigated and clarified. The methodology comprised analyses of tide gauge tsunami waveforms, spectral analyses, and numerical tsunami simulations. The main findings are summarized as follows.

1. The physical characteristics of the tsunami waveforms at all three tide gauge stations in southern Taiwan during the December 2006 tsunami were analyzed. The initial tsunami wave arrived at Kaohsiung, Dongkung, and Houbihu at 21:18, 20:54, and 20:42 national standard time, respectively, with a trough sign of tsunami amplitude. Following the initial wave trough, the initial wave crests were 0.07 m (Kaohsiung), 0.09 m (Dongkung), and 0.3 m (Houbihu). The maximum tsunami wave heights at the three tide gauge stations at Kaohsiung, Dongkung, and Houbihu were 0.08, 0.12, and 0.3 m, respectively, and the maximum tsunami wave heights at Kaohsiung and Dongkung were not recorded with the first waves. The approximate tsunami duration in Dongkung was 3.9 h, while the tsunami lasted for more than 6 h in Kaohsiung and Houbihu.
2. Based on the spectral analyses of tsunami waveforms, a period band of 13.6–23.1 min was attributed to the tsunami source spectrum. The periods of 16 and 36 min were considered the modes of trapped tsunami waves resonating with the fundamental modes of the shelves.
3. A tsunami source model for the 2006 earthquake doublet tsunami was proposed. The fault size of the successive earthquakes was estimated to be 800 km², comprising a length of 40 km and a width of 20 km. Uniform slips of 1.66 m (first earthquake, M_w 7.0) and 1.17 m (second earthquake, M_w 6.9) were estimated. The respective central fault depths of the two earthquakes were 20 and 33 km. The focal mechanisms of the first earthquake, with a strike of 319°, dip of 69°, and rake of −102°, and the second earthquake, with a strike of

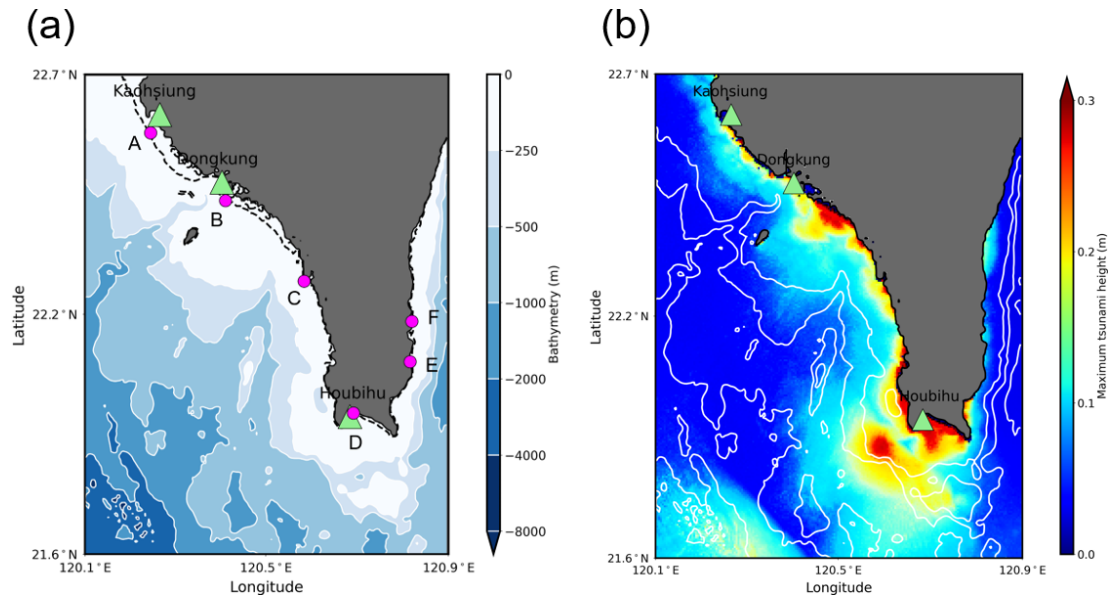


Figure 26. Zoomed map of the (a) bathymetry around southern Taiwan and (b) simulated maximum tsunami height using a multiple fault model (LS2). Green triangles indicate the locations of tide gauge stations, and pink circles denote numerical wave gauges at a sea depth of 20 m. The solid white lines are contour lines, and the dashed black line represents the bathymetric contour at a depth of 20 m.

151°, dip of 48°, and rake of 0°, could successfully produce the observed tsunami waveforms. Moreover, the tsunami sensitivity of the non-uniform fault slip distribution indicated that some tsunami signals might have been missing from the record signals due to the poor sampling rate (6 min intervals), and the wave peaks at Houbihu station might have reached twice the values of those observed during the 2006 tsunami.

4. A comparison of tsunami propagation simulations using actual (MS) and manipulated bathymetry (EXP1 and EXP2) revealed that the tsunami waves were coastally trapped during the passage of the 2006 tsunami. The trapped tsunami waves iteratively reflected and refracted among the shelves. The trapped waves interfered with incident waves and resonated with the fundamental modes of the shelves, resulting in an amplified and persistent oscillation of tsunami waves. This explained why the observed tsunami waves recorded at some stations in southern Taiwan were amplified and had a tsunami duration of more than 6 h during the 2006 tsunami.
5. Tsunamis are one of the most dangerous coastal hazards and can cause destructive damage and loss of life in coastal regions. Taiwan is at risk of tsunamis and is exposed to potential near-field tsunamis generated from the Manila Trench on the South China Sea (SCS) side and the Ryukyu Trench on the Pacific Ocean side. The results of the present study based on the 2006 tsunami revealed that the tsunami wave was trapped over the insular shelves around southern Taiwan during

the passage of the tsunami. Wave couplings and resonant features might result in unexpected amplification of tsunami heights and persistent wave oscillation in southern Taiwan. In other words, even if the initial wave heights are small, the tsunami waves that arrive later are expected to be higher and more persistent along the coast of southern Taiwan. Therefore, decision makers and people in southern Taiwan should be aware of this possibility and stay clear of coastal regions for a long time as an emergency response to future tsunamis, even if the wave height of an initially arriving tsunami wave is small. These findings are important and valuable for improving the existing system of tsunami warnings and coastal planning for disaster risk management.

7.2 Limitations and future improvements

In this study, the characteristics of the December 2006 tsunami and resulting tsunami behaviors in southern Taiwan were explored using available data from tide gauge tsunami waveforms and numerical tsunami simulations. Nevertheless, the analyses in this article had some limitations. The first limitation was related to the tsunami data recorded at the tide gauge stations, which were employed as input data for the spectral analyses (i.e., Fourier analyses and wavelet analyses) and compared with the numerical results. The sampling interval of the tide gauge data recorded at all CWB tide gauge stations was 6 min, indicating that tsunami wave components with shorter periods might not be well recorded in the tide gauge data. Due to this existing limitation, spectral analyses might cause discrepancies in detecting periodic components

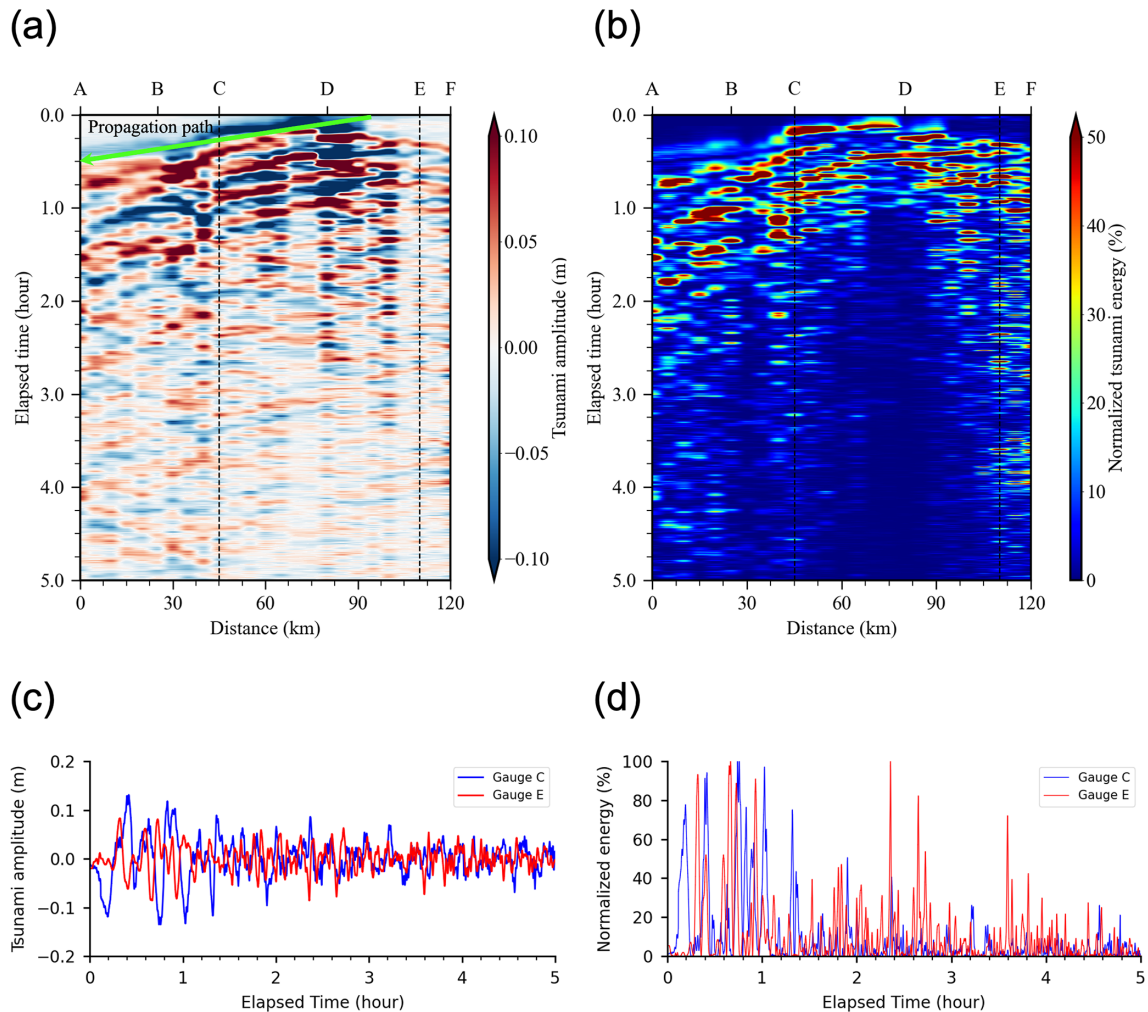


Figure 27. Time–distance diagram of the (a) tsunami wave and (b) normalized energy along the 20 m bathymetry contour from numerical wave gauges A to F and time series measurements of the (c) tsunami amplitude and (d) normalized energy at numerical wave gauges C and E. The dashed black lines indicate the distances of numerical wave gauges C and E from A. For interpretation of the references, please refer to Fig. 26a.

of tsunami spectra. This limitation could be improved by including tsunami data with more frequent sampling rates.

Another limitation was related to the simulation grid size (i.e., 450 m) for the tsunami propagation simulation. Although the simulated tsunami waveforms were reasonably consistent with the observed values recorded at the tide gauge stations in terms of wave amplitude and arrival time, the reproducibility of the numerical results for the 2006 tsunami could be further improved by constructing a finer grid of bathymetric data.

All the limitations mentioned above suggest further improvements to research to provide a more detailed investigation of long-lived edge wave and shelf resonance issues, especially in the region of southern Taiwan. In addition, more fundamental studies on the complex wave mechanisms of tsunami reflection and refraction, shoaling effects, and wave trapping by insular shelves are planned for future work.

Code and data availability. The second version of the TUNAMI code (TUNAMI-N2) used in this research is currently not an open-source model but is available from the corresponding author upon reasonable request. The recorded sea level data at tide gauge stations can be obtained from the Central Weather Bureau, R.O.C., through reasonable request. The seismic information is available in publicly accessible catalogs of the Global Centroid Moment Tensor (<https://www.globalcmt.org/CMTsearch.html>, last access: 14 January 2022; Global CMT, 2022) project and United States Geological Survey (https://earthquake.usgs.gov/earthquakes/eventpage/usp000f114#general_summary, last access: 14 January 2022; USGS, 2022a; https://earthquake.usgs.gov/earthquakes/eventpage/usp000f115/executive#general_summary, last access: 14 January 2022; USGS, 2022b), as mentioned in the body of the article. The topographic and bathymetric data of GEBCO and ETOPO1 used for the numerical tsunami simulations are publicly accessible at General Bathymetric Chart of the Ocean (https://www.gebco.net/data_and_products/gridded_bathymetry_data/, last access: 14 Jan-

uary 2022; GEBCO, 2022) and National Oceanic and Atmospheric Administration (<https://ngdc.noaa.gov/mgg/global/relief/ETOPO1/tiled/>, last access: 14 January 2022; NOAA, 2009).

Author contributions. All authors read, reviewed, and approved the manuscript. ACC wrote the manuscript, performed numerical simulation, and analyzed the results. FI and AS supervised the research and editing. KP provided constructive suggestions to the numerical simulation and the analyses of this study.

Competing interests. The contact author has declared that none of the authors has any competing interests.

Disclaimer. Publisher's note: Copernicus Publications remains neutral with regard to jurisdictional claims in published maps and institutional affiliations.

Special issue statement. This article is part of the special issue "Tsunamis: from source processes to coastal hazard and warning". It is not associated with a conference.

Acknowledgements. The authors thank Shyh-Fang Liu and Cheng-Lin Huang for their great support in collecting the observation data used in this work. The authors also thank Yo Fukutani from Kanto Gakuin University, Japan, for his valuable suggestions on conducting the sensitivity analysis of the fault models. We appreciate American Journal Expert for editing the draft of the manuscript.

Financial support. This research has been supported (in part) by the MEXT WISE Program for Sustainability in the Dynamic Earth.

Review statement. This paper was edited by Mohammad Heidarzadeh and reviewed by two anonymous referees.

References

- Cheng, S. N., Shaw, C. F., and Yeh, Y. T.: Reconstructing the 1867 Keelung earthquake and Tsunami based on historical documents, *Terr. Atmos. Ocean. Sci.*, 27, 431–449, [https://doi.org/10.3319/TAO.2016.03.18.01\(TEM\)](https://doi.org/10.3319/TAO.2016.03.18.01(TEM)), 2016.
- GEBCO: Global Ocean & land terrain models, GEBCO [code], https://www.gebco.net/data_and_products/gridded_bathymetry_data/, last access: 14 January 2022.
- Global CMT: CMT Catalog Citation Information, Global CMT [data set], <https://www.globalcmt.org/CMTsearch.html>, last access: 14 January 2022.
- Griffin, J., Latief, H., Kongko, W., Harig, S., Horspool, N., Hanung, R., Rojali, A., Maher, N., Fuchs, A., Hossen, J., Upi, S., Edi Dewanto, S., Rakowsky, N., and Cummins, P.: An evaluation of onshore digital elevation models for modeling tsunami inundation zones, *Front. Earth Sci.*, 3, 32, <https://doi.org/10.3389/feart.2015.00032>, 2015.
- Gusman, A. R., Satake, K., Shinohara, M., Sakai, S., and Tanioka, Y.: Fault Slip Distribution of the 2016 Fukushima Earthquake Estimated from Tsunami Waveforms, *Pure Appl. Geophys.*, 174, 2925–2943, <https://doi.org/10.1007/s00024-017-1590-2>, 2017.
- Harris, C. R., Millman, K. J., van der Walt, S. J., Gommers, R., Virtanen, P., Cournapeau, D., Wieser, E., Taylor, J., Berg, S., Smith, N. J., Kern, R., Picus, M., Hoyer, S., van Kerkwijk, M. H., Brett, M., Haldane, A., del Río, J. F., Wiebe, M., Peterson, P., Gérard-Marchant, P., Sheppard, K., Reddy, T., Weckesser, W., Abbasi, H., Gohlke, C., and Oliphant, T. E.: Array programming with NumPy, *Nature*, 585, 357–362, <https://doi.org/10.1038/s41586-020-2649-2>, 2020.
- Hayashi, Y., Koshimura, S., and Imamura, F.: Comparison of decay features of the 2006 and 2007 Kuril Island earthquake tsunamis, *Geophys. J. Int.*, 190, 347–357, <https://doi.org/10.1111/j.1365-246X.2012.05466.x>, 2012.
- Heidarzadeh, M. and Gusman, A. R.: Source modeling and spectral analysis of the Crete tsunami of 2nd May 2020 along the Hellenic Subduction Zone, offshore Greece, *Earth, Planets Sp.*, 73, 74, <https://doi.org/10.1186/s40623-021-01394-4>, 2021.
- Heidarzadeh, M. and Mulia, I. E.: Ultra-long period and small-amplitude tsunami generated following the July 2020 Alaska Mw 7.8 tsunamigenic earthquake, *Ocean Eng.*, 234, 109243, <https://doi.org/10.1016/j.oceaneng.2021.109243>, 2021.
- Heidarzadeh, M. and Satake, K.: Waveform and Spectral Analyses of the 2011 Japan Tsunami Records on Tide Gauge and DART Stations Across the Pacific Ocean, *Pure Appl. Geophys.*, 170, 1275–1293, <https://doi.org/10.1007/s00024-012-0558-5>, 2013.
- Heidarzadeh, M. and Satake, K.: Excitation of Basin-Wide Modes of the Pacific Ocean Following the March 2011 Tohoku Tsunami, *Pure Appl. Geophys.*, 171, 3405–3419, <https://doi.org/10.1007/s00024-013-0731-5>, 2014.
- Heidarzadeh, M. and Satake, K.: New Insights into the Source of the Makran Tsunami of 27 November 1945 from Tsunami Waveforms and Coastal Deformation Data, *Pure Appl. Geophys.*, 172, 621–640, <https://doi.org/10.1007/s00024-014-0948-y>, 2015.
- Heidarzadeh, M., Muhari, A., and Wijanarto, A. B.: Insights on the Source of the 28 September 2018 Sulawesi Tsunami, Indonesia Based on Spectral Analyses and Numerical Simulations, *Pure Appl. Geophys.*, 176, 25–43, <https://doi.org/10.1007/s00024-018-2065-9>, 2019.
- Heidarzadeh, M., Pranantyo, I. R., Okuwaki, R., Dogan, G. G., and Yalciner, A. C.: Long Tsunami Oscillations Following the 30 October 2020 Mw 7.0 Aegean Sea Earthquake: Observations and Modelling, *Pure Appl. Geophys.*, 178, 1531–1548, <https://doi.org/10.1007/s00024-021-02761-8>, 2021.
- Imamura, F.: Review of tsunami simulation with a finite difference method, in: Long-Wave Runup Models, edited by: Yeh, H., Liu, P., and Synolakis, C., World Scientific Publishing, Hackensack, NJ, 25–42, <https://doi.org/10.1142/9789814530330>, 1995.
- Kagan, Y. Y. and Jackson, D. D.: Worldwide doublets of large shallow earthquakes, *B. Seismol. Soc. Am.*, 89, 1147–1155, <https://doi.org/10.1785/bssa0890051147>, 1999.
- Kanamori, H. and Anderson, D. L.: Theoretical basis of some empirical relations in seismology, *B. Seismol. Soc. Am.*, 65, 1073–1095, 1975.

- Koshimura, S., Hayashi, Y., Munemoto, K., and Imamura, F.: Effect of the Emperor seamounts on trans-oceanic propagation of the 2006 Kuril Island earthquake tsunami, *Geophys. Res. Lett.*, 35, L02611, <https://doi.org/10.1029/2007GL032129>, 2008.
- Lay, T. and Kanamori, H.: Earthquake Doublets In The Solomon Islands, *Phys. Earth Planet. In.*, 21, 283–304, [https://doi.org/10.1016/0031-9201\(80\)90134-X](https://doi.org/10.1016/0031-9201(80)90134-X), 1980.
- Li, L., Switzer, A. D., Wang, Y., Weiss, R., Qiu, Q., Chan, C. H., and Tapponnier, P.: What caused the mysterious eighteenth century tsunami that struck the southwest Taiwan coast?, *Geophys. Res. Lett.*, 42, 8498–8506, <https://doi.org/10.1002/2015GL065567>, 2015.
- Li, L., Switzer, A. D., Chan, C. H., Wang, Y., Weiss, R., and Qiu, Q.: How heterogeneous coseismic slip affects regional probabilistic tsunami hazard assessment: A case study in the South China Sea, *J. Geophys. Res.-Sol. Ea.*, 121, 6250–6272, <https://doi.org/10.1002/2016JB013111>, 2016.
- Liu, P. L. F., Wang, X., and Salisbury, A. J.: Tsunami hazard and early warning system in South China Sea, *J. Asian Earth Sci.*, 36, 2–12, <https://doi.org/10.1016/j.jseaes.2008.12.010>, 2009.
- Liu, T.-C., Wu, T.-R., and Hsu, S.-K.: Historical tsunamis of Taiwan in the 18th century: the 1781 Jiateng Harbor flooding and 1782 tsunami event, *Nat. Hazards Earth Syst. Sci.*, 22, 2517–2530, <https://doi.org/10.5194/nhess-22-2517-2022>, 2022.
- Ma, K. F. and Liang, W. T.: Preface to the 2006 Pingtung Earthquake Doublet Special Issue, *Terr Atmos. Ocean. Sci.*, 19, I–III, [https://doi.org/10.3319/TAO.2008.19.6.I\(PT\)](https://doi.org/10.3319/TAO.2008.19.6.I(PT)), 2008.
- Masaya, R., Suppasri, A., Yamashita, K., Imamura, F., Gouramanis, C., and Leelawat, N.: Investigating beach erosion related with tsunami sediment transport at Phra Thong Island, Thailand, caused by the 2004 Indian Ocean tsunami, *Nat. Hazards Earth Syst. Sci.*, 20, 2823–2841, <https://doi.org/10.5194/nhess-20-2823-2020>, 2020.
- Megawati, K., Shaw, F., Sieh, K., Huang, Z., Wu, T. R., Lin, Y., Tan, S. K., and Pan, T. C.: Tsunami hazard from the subduction megathrust of the South China Sea: Part I. Source characterization and the resulting tsunami, *J. Asian Earth Sci.*, 36, 13–20, <https://doi.org/10.1016/j.jseaes.2008.11.012>, 2009.
- Munger, S. and Cheung, K. F.: Resonance in Hawaii waters from the 2006 Kuril Islands Tsunami, *Geophys. Res. Lett.*, 35, L07605, <https://doi.org/10.1029/2007GL032843>, 2008.
- NOAA: ETOPO1 1 Arc-Minute Global Relief Model, National Geophysical Data Center, NOAA National Centers for Environmental Information [code], <https://ngdc.noaa.gov/mgg/global/relief/ETOPO1/tiled/> (last access: 14 January 2022), 2009.
- Nosov, M. A., Bolshakova, A. V., and Kolesov, S. V.: Displaced Water Volume, Potential Energy of Initial Elevation, and Tsunami Intensity: Analysis of Recent Tsunami Events, *Pure Appl. Geophys.*, 171, 3515–3525, <https://doi.org/10.1007/s00024-013-0730-6>, 2014.
- Okada, Y.: Surface deformation due to shear and tensile faults in a half-space, *B. Seismol. Soc. Am.*, 75, 1135–1154, <https://doi.org/10.1785/BSSA0750041135>, 1985.
- Otake, T., Chua, C. T., Suppasri, A., and Imamura, F.: Justification of possible casualty-reduction countermeasures based on global tsunami hazard assessment for tsunami-prone regions over the past 400 years, *J. Disaster Res.*, 15, 490–502, <https://doi.org/10.20965/jdr.2020.p0490>, 2020.
- Papazachos, B. C., Scordilis, E. M., Panagiotopoulos, D. G., Papazachos, C. B., and Karakaisis, G. F.: Global Relations between seismic fault parameters and moment magnitude of earthquakes, *Bulletin of the Geological Society of Greece*, 36, 1482–1489, <https://doi.org/10.12681/bgsg.16538>, 2004.
- Qiu, Q., Li, L., Hsu, Y.-J., Wang, Y., Chan, C.-H., and Switzer, A. D.: Revised earthquake sources along Manila trench for tsunami hazard assessment in the South China Sea, *Nat. Hazards Earth Syst. Sci.*, 19, 1565–1583, <https://doi.org/10.5194/nhess-19-1565-2019>, 2019.
- Rabinovich, A. B.: Spectral analysis of tsunami waves: Separation of source and topography effects, *J. Geophys. Res.-Oceans*, 102, 12663–12676, <https://doi.org/10.1029/97JC00479>, 1997.
- Rabinovich, A. B., Candella, R. N., and Thomson, R. E.: The open ocean energy decay of three recent trans-Pacific tsunamis, *Geophys. Res. Lett.*, 40, 3157–3162, <https://doi.org/10.1002/grl.50625>, 2013.
- Ren, Z., Liu, H., Jimenez, C., and Wang, Y.: Tsunami resonance and standing waves in the South China Sea, *Ocean Eng.*, 262, 112323, <https://doi.org/10.1016/j.oceaneng.2022.112323>, 2022.
- Roeber, V., Yamazaki, Y., and Cheung, K. F.: Resonance and impact of the 2009 Samoa tsunami around Tutuila, American Samoa, *Geophys. Res. Lett.*, 37, L21604, <https://doi.org/10.1029/2010GL044419>, 2010.
- Sugawara, D., Yu, N. T., and Yen, J. Y.: Estimating a Tsunami Source by Sediment Transport Modeling: A Primary Attempt on a Historical/1867 Normal-Faulting Tsunami in Northern Taiwan, *J. Geophys. Res.-Earth Surf.*, 124, 1675–1700, <https://doi.org/10.1029/2018JF004831>, 2019.
- Sun, Y.-S., Chen, P.-F., Chen, C.-C., Lee, Y.-T., Ma, K.-F., and Wu, T.-R.: Assessment of the peak tsunami amplitude associated with a large earthquake occurring along the southernmost Ryukyu subduction zone in the region of Taiwan, *Nat. Hazards Earth Syst. Sci.*, 18, 2081–2092, <https://doi.org/10.5194/nhess-18-2081-2018>, 2018.
- Suppasri, A., Futami, T., Tabuchi, S., and Imamura, F.: Mapping of historical tsunamis in the Indian and Southwest Pacific Oceans, *Int. J. Disaster Risk Reduct.*, 1, 62–71, <https://doi.org/10.1016/j.ijdr.2012.05.003>, 2012.
- Suppasri, A., Muhari, A., Futami, T., Imamura, F., and Shuto, N.: Loss Functions for Small Marine Vessels Based on Survey Data and Numerical Simulation of the 2011 Great East Japan Tsunami, *J. Waterw. Port C. Div.*, 140, 5, [https://doi.org/10.1061/\(asce\)ww.1943-5460.0000244](https://doi.org/10.1061/(asce)ww.1943-5460.0000244), 2014.
- Suppasri, A., Leelawat, N., Latcharote, P., Roeber, V., Yamashita, K., Hayashi, A., Ohira, H., Fukui, K., Hisamatsu, A., Nguyen, D., and Imamura, F.: The 2016 Fukushima earthquake and tsunami: Local tsunami behavior and recommendations for tsunami disaster risk reduction, *Int. J. Disast. Risk Reduct.*, 21, 323–330, <https://doi.org/10.1016/j.ijdr.2016.12.016>, 2017.
- Tanioka, Y. and Satake, K.: Tsunami generation by horizontal displacement of ocean bottom, *Geophys. Res. Lett.*, 23, 861–864, <https://doi.org/10.1029/96GL00736>, 1996.
- Tanioka, Y., Shibata, M., Yamanaka, Y., Gusman, A. R., and Ioki, K.: Generation mechanism of large later phases of the 2011 Tohoku-oki tsunami causing damages in Hakodate, Hokkaido, Japan, *Prog. Earth Planet. Sci.*, 6, 30, <https://doi.org/10.1186/s40645-019-0278-x>, 2019.

- Torrence, C. and Compo, G. P.: A Practical Guide to Wavelet Analysis, *B. Am. Meteorol. Soc.*, 79, 61–78, [https://doi.org/10.1175/1520-0477\(1998\)079<0061:APGTWA>2.0.CO;2](https://doi.org/10.1175/1520-0477(1998)079<0061:APGTWA>2.0.CO;2), 1995.
- USGS: M 7.1 – 30 km SW of Hengchun, Taiwan, USGS [data set], https://earthquake.usgs.gov/earthquakes/eventpage/usp000f114#general_summary, last access: 14 January 2022.
- USGS: M 6.9 – 26 km W of Hengchun, Taiwan, USGS [data set], https://earthquake.usgs.gov/earthquakes/eventpage/usp000f115/executive#general_summary, last access: 14 January 2022.
- Wang, Y., Zamora, N., Quiroz, M., Satake, K., and Cienfuegos, R.: Tsunami Resonance Characterization in Japan Due to Trans-Pacific Sources: Response on the Bay and Continental Shelf, *J. Geophys. Res.-Oceans*, 126, e2020JC017037, <https://doi.org/10.1029/2020JC017037>, 2021.
- Wang, Y., Su, H. Y., Ren, Z., and Ma, Y.: Source Properties and Resonance Characteristics of the Tsunami Generated by the 2021 M 8.2 Alaska Earthquake, *J. Geophys. Res.-Oceans*, 127, e2021JC018308, <https://doi.org/10.1029/2021JC018308>, 2022.
- Wu, T. R. and Huang, H. C.: Modeling tsunami hazards from Manila trench to Taiwan, *J. Asian Earth Sci.*, 36, 21–28, <https://doi.org/10.1016/j.jseaes.2008.12.006>, 2009.
- Wu, T. R., Chen, P. F., Tsai, W. T., and Chen, G. Y.: Numerical study on tsunamis excited by 2006 Pingtung earthquake doublet, *Terr. Atmos. Ocean. Sci.*, 19, 705–715, [https://doi.org/10.3319/TAO.2008.19.6.705\(PT\)](https://doi.org/10.3319/TAO.2008.19.6.705(PT)), 2008.
- Wu, Y. M., Zhao, L., Chang, C. H., Hsiao, N. C., Chen, Y. G., and Hsu, S. K.: Relocation of the 2006 Pingtung Earthquake sequence and seismotectonics in Southern Taiwan, *Tectonophysics*, 479, 19–27, <https://doi.org/10.1016/j.tecto.2008.12.001>, 2009.
- Yamanaka, Y. and Nakamura, M.: Frequency-dependent amplification of the Sanriku tsunamis in Ryori Bay, *Earth, Planets Sp.*, 72, 6, <https://doi.org/10.1186/s40623-019-1128-1>, 2020.
- Yamazaki, Y. and Cheung, K. F.: Shelf resonance and impact of near-field tsunami generated by the 2010 Chile earthquake, *Geophys. Res. Lett.*, 38, L12605, <https://doi.org/10.1029/2011GL047508>, 2011.
- Zengaffinen, T., Lovholt, F., Pedersen, G. K., and Muhari, A.: Modelling 2018 Anak Krakatoa Flank Collapse and Tsunami: Effect of Landslide Failure Mechanism and Dynamics on Tsunami Generation, *Pure Appl. Geophys.*, 177, 2493–2516, <https://doi.org/10.1007/s00024-020-02489-x>, 2020.